Electrode Geometry Effects on Plume Characteristics and Thruster Performance of ZaP-HD

Jared Smythe

A thesis
submitted in partial fulfillment of the
requirements for the degree of

Master of Science in Aeronautics & Astronautics

University of Washington

2023

Reading Committee:
Uri Shumlak, Chair
Justin Little

Program Authorized to Offer Degree:
Aeronautics and Astronautics

University of Washington

Abstract

Electrode Geometry Effects on Plume Characteristics and Thruster Performance of ZaP-HD

Jared Smythe

Chair of the Supervisory Committee:
Uri Shumlak
Aeronautics and Astronautics

The addition of sheared-flow stabilization (SFS) to a Z-pinch configuration has allowed increased stability and plasma lifetime. This shows great promise for use as a compact, linear, fusion device and as a future deep space propulsion engine. Previous theses have examined the feasibility of this endeavor with promising results. For such a device, an understanding of how the physical geometry can change thruster and pinch performance would be required. To begin this investigation, the end wall electrode geometry was altered on the University of Washington's Z-Pinch High Density (ZaP-HD) experiment. Thruster parameters were determined through plume characterization utilizing simultaneous measurements of electron temperature and density by way of a triple Langmuir probe. This method allowed for performance parameters to be resolved in time and space through a multitude of shots. The Langmuir probe revealed a radially uniform temperature plume with peak electron temperatures of 60 eV and number densities on the order of 10^{20} m^{-3}. These measurements were supplemented by ion Doppler spectroscopy to determine flow speeds of up to 103 km/s with an open configuration and 27 km/s on the more restrictive electrode geometry. Thruster performance metrics of thrust and specific impulse are extrapolated from these measurements: 123 mN with 16,000 s I_{sp}, 824 μN with 7,000 s I_{sp}, and 252 μN with 6,500 s I_{sp} for the respective configurations of no, spoked and original end wall.

TABLE OF CONTENTS

LIST OF FIGURES

LIST OF TABLES

ACKNOWLEDGEMENTS

I would like to thank my lab mates Aqil Khairi, Bennett Diamond, Harry Furey-Soper, Shane Murray, Zhangsheng Lian and Jeff Peachman for assisting me in run campaigns and keeping the lab/office space a lively, enjoyable environment. A special shout out goes to Aqil and John Rogers for helping me constantly remove the vacuum extension and go through the pain staking process of realigning it. A massive thanks goes to my advisor, Uri Shumlak, for his guidance on my master's research journey. I would also like to thank my ski squad for all the fun times in the mountains that kept me sane in between run campaigns. Last, but certainly not least, I would like to thank my parents for their unwavering support of me through my academic journey.

DEDICATION

This body of work is dedicated to my late father, John.

Chapter 1

INTRODUCTION

A successful fusion device has many extraordinary possible implementations for humanity. It promises a clean and abundant energy source to quench a growing energy demand. Z pinches were one of the most promising fusion configuration devices in fusion research's infancy due to its simplicity. The rampant instabilities that were quickly realized put the Z-pinch configuration on the back burner in favor of more stable configurations such as a tokamak, magnetic mirror, stellerator or field-reversed configuration (FRC). In the past few decades, the Z pinch has made a return with the addition of sheared-flow stabilization (SFS). Like all of the aforementioned configurations, the Z pinch utilizes magnetic confinement. The simplistic nature of the pure Z pinch is attractive in that it does not require any external magnetic field coils. The magnetic field is self generated by the plasma. This reduces complexity greatly as these external field coils are often heavy, super conducting magnetic coils. Other fusion configurations utilize these external magnetic field coils to mitigate inherent instabilities in the plasma such as the Rayleigh-Taylor instability or "sauge" mode (m=0) and the "kink" (m=1). A Z pinch can mitigate these instabilities through the introduction of sheared flow as seen in Fig 1.1.

The mitigation of these instabilities is crucial for the goal of obtaining break-even nuclear fusion. Once this break-even point has been reached, not only will this allow for a compact fusion device, but also promises a possibility for a high performance deep space propulsion device due to its linear nature. This could help solve the propulsion issue humanity is faced with when attempting to explore our own solar system.

To enable human travel to celestial bodies of scientific interest such as Mars, Europa, and Enceladus, a new method of propulsion needs to be realized. Tab. 1.1 illustrates

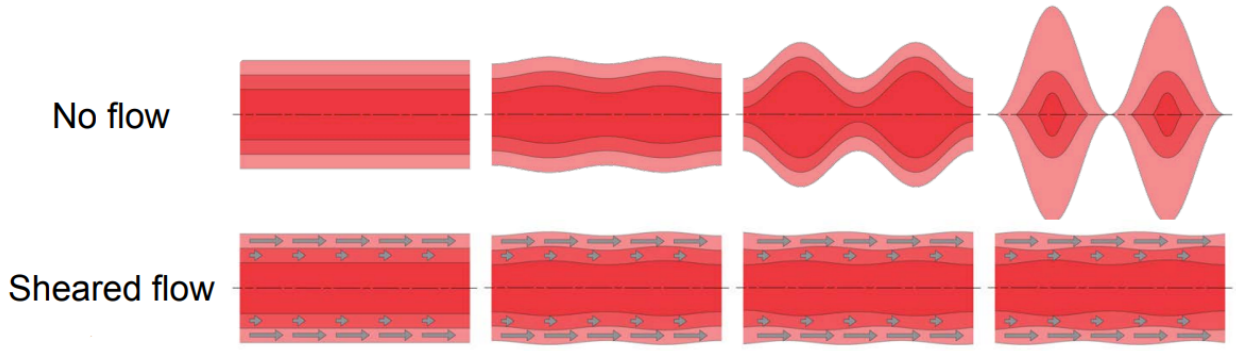

Figure 1.1: Illustration of the stabilizing characteristics of shear flow to the m=0 sausage instability in a Z pinch. [9]

the long times it takes to reach these distance locations. Current chemical rockets can provide the necessary thrust needed for crewed missions but lack the efficiency required. This combination leads to enormous spacecraft that are mostly composed of fuel. State of the art electric propulsion provides the needed efficiency for deep space travel but offers minimal thrust. This is acceptable for probes as they are not constrained by transit times and can spend many years getting to their destination. Large clusters of electric propulsion engines would be required to propel a crewed mission. Increased complexity and failure modes is not ideal for a manned mission. Long exposure to deep space and its radiation is detrimental to humans. While shielding can be provided on the spacecraft, this adds tremendous weight, further increasing the propellant requirements. These issues necessitate a propulsion device that can offer the same thrust levels of chemical rockets with efficiencies at or beyond what is seen in electric propulsion. This would allow fast transit times while keeping the mass of the propulsion system low. The mass reduction in the propulsion system would enable more mass to be available to the payload.

Destination	Typical Transit Time
Mars	7 months
Europa	5-6 years
Enceladus	7 years

Table 1.1: Tabulated values demonstrating the long transit times it takes to get to a few scientifically interesting bodies in our solar system. All of these times are quite long for humans to be subjected to the environment of interplanetary space. Times provided by various NASA missions [2, 6].

1.1 The Z-Pinch High Density Experiment (ZaP-HD)

The original sheared flow Z-Pinch experiment at the University of Washington was known as ZaP, and only had an inner and outer electrode in addition to a longer compression region. The next iteration was FuZE, which shortened the assembly region to that of the eventual ZaP-HD and strove to push the plasma parameters of ZaP. The most recent iteration of the sheared-flow Z pinch is ZaP-HD. A cross section of which can be seen in Fig. 1.2. This configuration added a middle electrode. This three electrode design aims to increase the plasma parameters even further. Specifically, its goal is to increase the plasma's density, hence the high density portion of the name. Having three electrodes enables ZaP-HD to introduce more energy into the plasma in the compression region. This is achieved by delaying the time in which the compression voltage is applied in comparison to the acceleration voltage. The exact operation and merits of this approach are illustrated and described in Fig. 1.3.

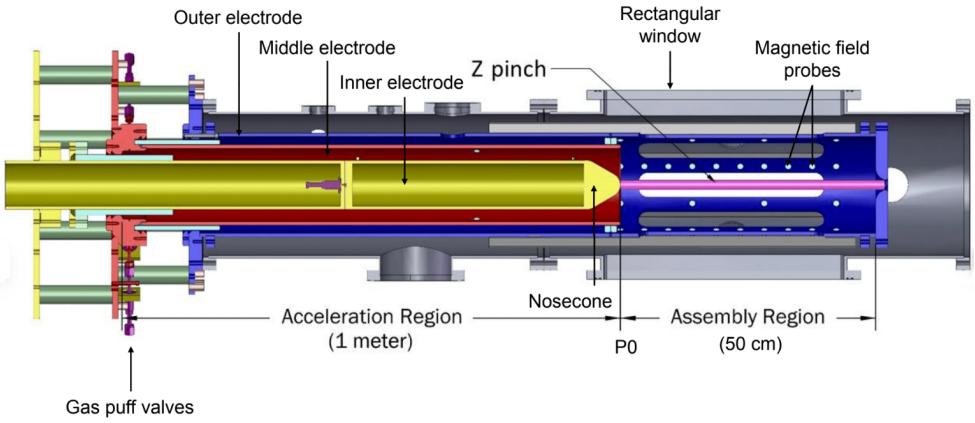

Figure 1.2: Cross section view of the ZaP-HD flow Z-Pinch Experiment. Plasma is accelerated in the acceleration region. It is further confined into a sheared-flow stabilized Z pinch in the assembly region. It is then exhausted out into the vacuum chamber.

1.2 Goals and Approach

This thesis aims to build upon the work of the Parson MS thesis, where examination of the feasibility of using FuZE as a space propulsion device was completed. It was found that a hypothetical space thruster using FuZE would a have specific impulse close to 9000 s and a thrust near 1400 N [15]. In addition, the plume of FuZE tended to be well collimated which is preferred for a space propulsion device. Ref. [10] performed preliminary measurements on the plume on ZaP-HD. These measurements found that ZaP-HD had a plume with a 15 degree divergence angle [10]. It is worth noting that the FuZE end wall was an 8-spoke wagon wheel design whereas ZaP-HD's end wall is a solid round with a hole in the center. This geometry difference may lead one to expect a difference in plume and thrust characteristics. That thought is the driving force behind this thesis. To examine this idea, three different end wall geometries are tested: original, no end wall, 4 spoke. The specific parameter being analyzed is the flow through percentage of the end wall geometry, with no end wall corresponding to a flow through percentage of 100. Ultimately a trend between thruster

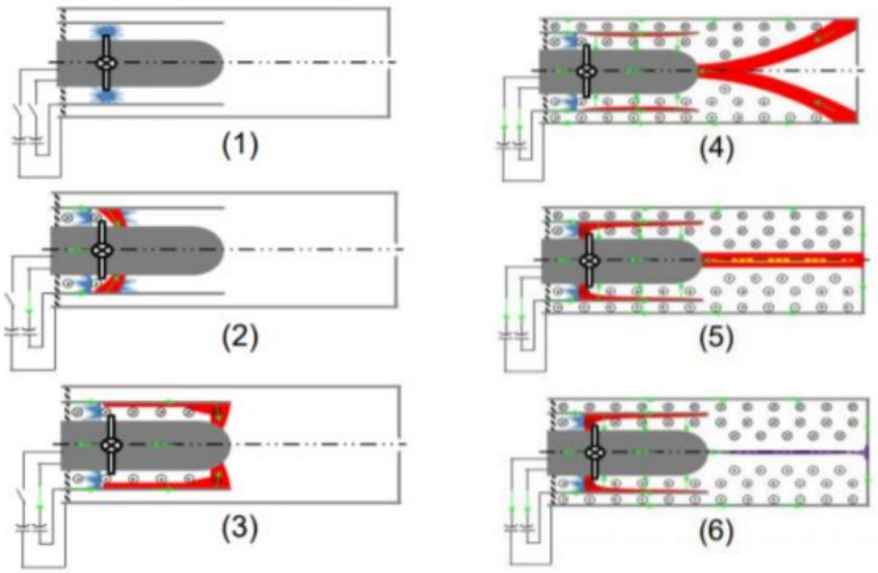

Figure 1.3: A pulse starts by injecting gas into the annual region between the inner and middle electrode from gas puff valves (1). A voltage is then applied between said electrodes, creating a breakdown of the gas into plasma (2). This in turn creates a current and subsequent magnetic field. This accelerates the plasma down the channel via the $\vec{j} \times \vec{B}$ force (3). Once the plasma reaches the compression region, a second voltage is then applied between the outer electrode and the inner (4). This drives additional current through the plasma helping to confine and compress the plasma further (5-6) [7].

performance, plume characteristics and end wall flow through area/geometry is analyzed. To this end, both a triple Langmuir probe and ion Doppler spectroscopy (IDS) are used. A triple Langmuir probe allows for both three-dimensional spatial resolution as well as time resolution of plasma parameters in the plume. The Langmuir probe is mounted on a translation stage that allows changing its radial location from the machine axis to the outer extent of the vacuum chamber. Additionally, the vacuum extension has multiple ports spaced along the z-axis on which the probe can be mounted. This allows for a full three dimensional characterization of the plume, albiet at a relatively low spatial resolution due to port spacing. IDS is used to find the speed of the ions in the plume. While this measurement is spatially resolved in the radial direction, it is not time or other dimensionally resolved. Despite these limitations, IDS is used instead of a quadruple Langmuir probe (mach probe) due to the low SNR and unreliable results as stated in Ref. [15]. Between these two diagnostics, a full characterization of the plume is done.

Chapter 2

THEORY

Langmuir Probes and ion Doppler spectroscopy are used to evaluate the properties and characteristics of ZaP-HD's plume. From these two diagnostics, it is possible to calculate electron temperature, density and ion speed. This chapter outlines the physics foundation of these diagnostics and how these plasma properties are calculated from experimental data.

2.1 Langmuir Probes

Langmuir Probes are a particular subset of plasma diagnostic tools that are under the category of perturbing electrostatic diagnostics. Langmuir probes operate on the concept of ion collection in sheath theory. While there are many sheath theories depending on the exact application, this experiment uses thin sheath theory. A representation of this type of sheath can be seen in Fig. 2.1.

A way to make a rudimentary probe is to insert an insulated wire, with its tip exposed, into the plasma and measure a characteristic curve known as the I-V characteristic, Fig. 2.2. The I-V characteristic is broken down into three distinct regions: ion saturation current, transition region and electron saturation current [4]. The far left of the curve is where the ion saturation current can be seen. In this region, the bias is sufficiently negative such that all of the electrons are repelled and only an ion current flows. Likewise, the far right of the curve shows the electron saturation current due to a sufficiently positive bias such that all the ions are repelled. These two regions are joined by the transition region which is the exponential part of the I-V curve. It is in this region that the electron temperature can be extracted through examination of the slope near the floating potential.

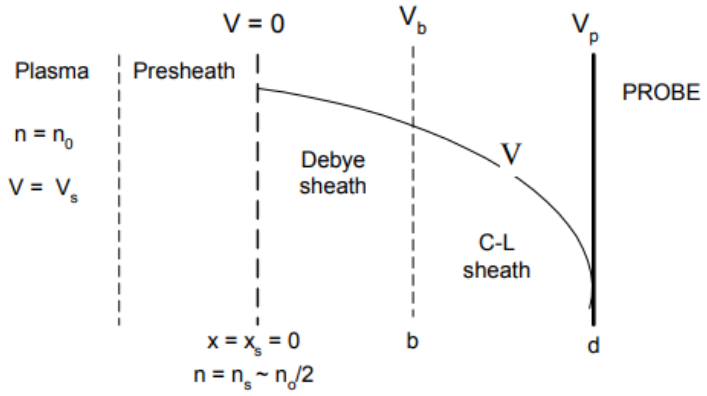

Figure 2.1: Make-up of the sheath regions. The scales are greatly exaggerated for ease of visual understanding [4].

2.1.1 Single Probes

A single Langmuir probe is the most simplistic probe, but requires a more complicated circuit. Because there is only one electrode in this system, only one point on the I-V curve can be measured at a time. The bias voltage on the Langmuir probe must be swept by a circuit in order to trace the I-V characteristic. Many plasma properties can be obtained from this I-V characteristic. The plasma floating potential, which as defined as the point where no current flows, can be easily found by the x-intercept of the graph. The slope of the transition region and the electron saturation current define the "knee" of the curve. This point aligns with the plasma potential. The transition region also allows for the calculation of electron temperature by examining the inverse of the log of the slope. While simple, single probes have the major disadvantage of needing a sweep time. Although many fast sweeping circuits do exist, these circuits are often very expensive and complex. Because of this, highly dynamical plasmas that have a fast very potential create a challenge for using the Langmuir probe diagnostic.

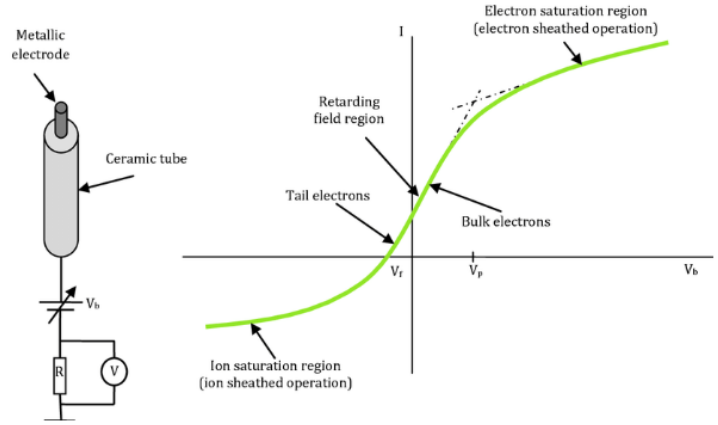

Figure 2.2: A typical I-V characteristic curve from a single Langmuir probe. This trace is created by sweeping the voltage from sufficiently negative value so the probe only collects ions, $I_{i,sat}$ to sufficiently high voltage such that the same is true for electrons, $I_{e,sat}$.

2.1.2 Triple Probes

A triple Langmuir probe is able to overcome the shortcomings of a single probe in highly dynamical plasmas. It achieves this by utilizing three electrodes instead of one. It builds off of a double probe, by adding a third floating probe. A double probe operates with two electrodes that have a bias applied between them. Adding a floating probe allows the simultaneous determination of electron temperature and density. This eliminates the need for sweeping the voltage and thus the measurements can keep up with fast varying plasma potentials. The three electrode design allows for operation in both a current mode and voltage mode. The diagnostic set up used on ZaP-HD is in the voltage mode configuration so that will be discussed in detail. The voltage mode setup can been seen in Fig. 2.3 along with how the voltages compare relative to one another as well as relative plasma voltages. Since the second electrode is electrically isolated from the other pair and not biased, it is allowed to float to the plasma floating potential. The other pair of electrodes are given a fixed bias, V_{d3}. This bias is chosen to be sufficiently negative such that one probe tip will

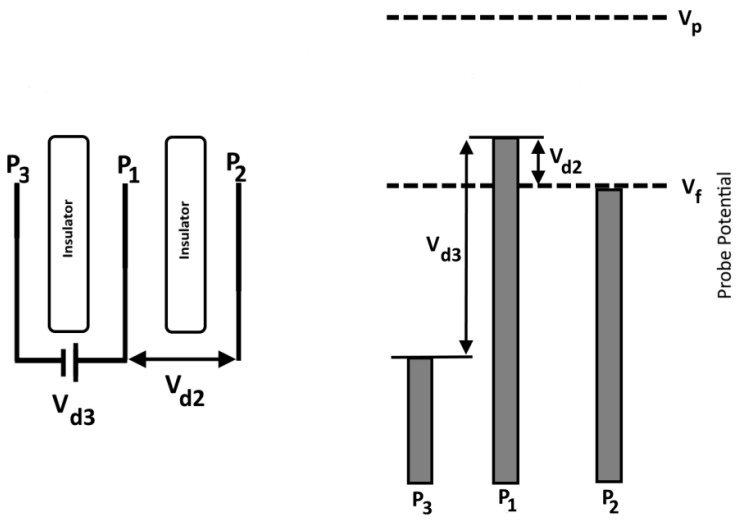

Figure 2.3: Simplified electrical and relative potentials of a triple Langmuir probe. P_2 is utilized as a floating probe in conjunction with the P_1, P_3 double probe pair. The arrows between P_1 and P_2 indicate a measurement of voltage, not an electrical connection.

collect the ion saturation current. It is also important to note that the current of these electrodes is the same due to current continuity. This fact is used in the later sections to calculate electron temperature and density.

In experiments conducted by Ref. [14], it has been found that the current operation of a triple probe is less susceptible to EMI than the voltage mode configuration. However, the triple probe previously used was in voltage mode and so it was deemed easiest to continue this mode of operation despite its short comings.

Electron Temperature Determination

Knowledge of the temperature of the electrons in a plasma is a very important parameter to calculate. Overall, plasma temperature is often based on electron temperature since many plasmas are assumed to be thermalized. Other parameters such as electron density also require knowledge of the temperature. As stated previously, a current balance and

continuity is used to calculate electron parameters. The current through each probe can be written as

$$I_1 = I_{i0} + I_{e0} \exp\left(-\frac{eV_1}{kT_e}\right) \tag{2.1}$$

$$I_2 = I_{i0} + I_{e0} \exp\left(-\frac{eV_2}{kT_e}\right) \tag{2.2}$$

$$I_3 = I_{i0} + I_{e0} \exp\left(-\frac{eV_3}{kT_e}\right) \tag{2.3}$$

I_2 is set to zero since that probe is floating and thus the flux of electrons and ions is equal [4, 13]. I_1 and I_3 are negatives of each other because they are part of the same series circuit. Dividing Eq. (2.1) by Eq. (2.3) and substituting in Eq. (2.2),

$$2\exp\left(-\frac{eV_{d2}}{k_B T_e}\right) = 1 + \exp\left(-\frac{eV_{d3}}{k_B T_e}\right), \tag{2.4}$$

which is a transcendental function that can be solved numerically for electron temperature where V_{d2} corresponds to the difference between the first electrode and second electrode voltage and so on. There are some linear approximations that can be used to simplify this expression into one that is analytical. This approach was not used here due to the divergence from true temperature values that Ref. [15] performed. Additionally, there are some key assumptions that are made to perform this calculation. The probe is assumed to be in the collisionless regime. This implies that the radius of the probe is much less than that of the mean free path of the particles. It is also required that the sheath itself is collisionless, dictating that the Debye length be much smaller than the radius of the probe. Lastly, the probe collection area must be equal for all electrodes.

Electron Density Determination

While the electron temperature can be directly measured by examining features of the I-V characteristic, electron number density cannot be directly measured from a Langmuir probe. This is due to the probe being limited to the ion saturation current. It can, however, be

calculated with the knowledge of electron temperature and ion saturation current.

$$I_{i0} = 0.61 n_e e S \sqrt{\frac{kT_e}{m_i}} \tag{2.5}$$

These two parameters are related to the density through Eq. (2.5) [13]. This equation can be combined with Eq. (2.1) and Eq. (2.2) to produce an equation for electron number density in terms of known parameters from the triple Langmuir probe.

$$n_e = \frac{I_3}{\exp(-1/2) S e \sqrt{\frac{k_B T_e}{m_i}}} \frac{\exp(-\frac{eV_{d2}}{k_B T_e})}{1 - \exp(-\frac{eV_{d2}}{k_B T_e})} \tag{2.6}$$

This equation is very sensitive to when the voltage difference between probe one and two is small due to the negative exponential. Likewise, it is also sensitive to when the plasma has very hot electrons. The former is of importance since this difference will cross through zero as the plasma nears the end of its life, causing non-physical results in electron density. To combat this, I-V characteristics can be traced during any suspect time to ensure physical results.

2.2 Ion Doppler Spectroscopy (IDS)

Many people have experience with the Doppler effect. As a vehicle approaches, its sound appears higher pitched. When said vehicle moves away, it appears to be pitched down. This is caused by sounds waves compressing for the former and stretching for the latter. Police exploit this phenomena to measure how fast a car is moving. The same physics that is in a radar gun to determine a vehicles speed can also be used to determine the speed of ions in the plasma.

2.2.1 Line Radiation

Instead of using an external EM-wave source like in a radar gun, IDS relies on line radiation from impurities in the plasma itself. This is very convenient as nothing additional is required of this diagnostic other than observing the plasma. Line radiation occurs when an excited

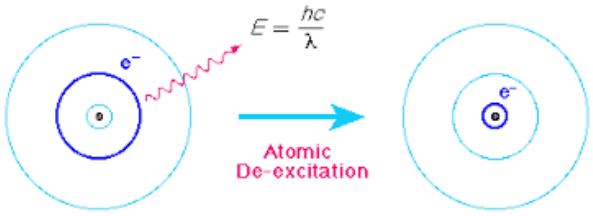

Figure 2.4: Electron orbital energy transition of a generic atom showing the initial and final energy states of the electron.

electron in an impurity ion de-excites and releases a photon, Fig. 2.4. These de-excitation events release a photon at a unique energy level and therefore wavelength due to the electron energy levels being quantized. National Institute of Standards and Technology (NIST) has a spectral database listing all elements and what wavelengths they emit depending on their ionization state and which specific transition occurs. This is very useful when comparing shifted wavelengths from IDS. Since the makeup of the ZaP-HD plasma is known, a specific line radiation peak can be chosen to observe its Doppler shift.

2.2.2 Speed determination

By looking at a non-perpendicular angle to the plasma flow, a portion of the viewed bulk movement will either be red or blue shifted. This implies that the viewed spectral line will not appear at the same wavelength as a stationary emitting ion. This shift in wavelength is directly proportional to its speed. A larger shift corresponds to a higher speed.

$$v = c\left(\frac{\Delta\lambda}{\lambda_0}\right)\frac{1}{cos(\theta)} \tag{2.7}$$

The velocity can be determined through, Eq. (2.7), where $\Delta\lambda$ is the shift in wavelength and λ_0 is the wavelength that would be observed from a stationary ion. The observation angle dependence is taken into account via $cos(\theta)$, where θ is the viewing angle from the axis of velocity.

Chapter 3
EXPERIMENTAL SETUP

Thruster performance of ZaP-HD was analyzed through the use of a triple Langmuir probe and ion Doppler spectroscopy. The theory of these diagnostics was outline in the previous theory section. This chapter serves to delve into how these tools were utilized on the ZaP-HD experiment and offer reasoning for specific configuration decisions. A vacuum extension vessel originally used for FuZE was equipped on ZaP-HD to facilitate the probing of the plasma exhaust, Fig. 3.1. Any z measurement is in reference to a distance from the exit plane of the end wall electrode. A P measurement is referenced from the nosecone of ZaP-HD.

3.1 Langmuir Probe Setup

A quadruple Langmuir probe had previously been used on ZaP-HD and her sister experiment FuZE in the past. A quadruple probe is nothing more than a triple probe with the addition of a mach probe. This mach probe was used by the Parson MS thesis to estimate the speed of the plume on FuZE. Ref. [15] analysis found that the signal to noise ratio is far too low and thus reliable data could not be determined from this setup [15]. This is the motivation behind only using the probe in a triple configuration and relying on IDS for speed measurements. A triple probe configuration was chosen for its advantages in measuring plasmas with quickly varying potentials and those plasmas with short lifetimes.

The Langmuir probe electrical circuit needed some repairs before it could be operational. After numerous repairs, reliable data was still not being recorded. This necessitated re-examining the complexity of the original Langmuir probe circuit. It implemented op-amps in a unity gain buffer configuration to help isolate the output to the oscilloscope from the

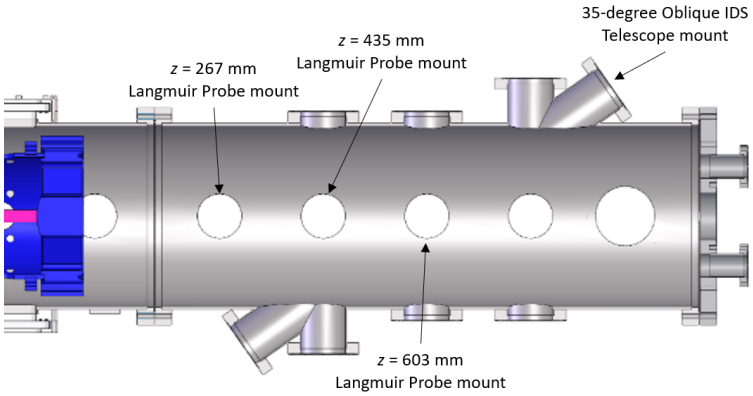

Figure 3.1: Vacuum extension vessel used on ZaP-HD. This allowed the plume to fully develop and not be obstructed by a short end chamber. The end wall electrode can be seen at left in blue.

plasma signals. The worry was that any large spikes in plasma signals could damage the oscilloscope. The drawback of this approach was that it added high frequency electronic noise from the active nature of said op-amps. Langmuir probe signals often have relatively low signal to noise ratio, so additional high frequency noise is problematic. The other main features of the circuit were voltage dividers and a capacitor cluster between the double probe portion of the circuit. The voltage dividers were in place to reduce the voltage signal seen in the oscilloscope as the double probe was biased to 200 V and that is far higher than the oscilloscope can handle. The group of capacitors helped aid in the delivery of a more constant voltage to the double probe tip. This is needed because the plasma will attempt to drop this voltage quickly by drawing out charges and the high voltage power supply cannot response sufficiently fast. Without capacitors in the circuit, the probe would experience voltage collapse, meaning the measured voltage would be zero. The op-amps were taken out of the circuit in an attempt to simplify the circuit and gather data with higher signal to noise ratio. The voltage dividers were deemed sufficient to protect the oscilloscope.

The oscilloscope being used is a Tektronix MDO-3014 model. This allows for up to 2.5 GHz sampling rate and variable input impedance which is important for impedance

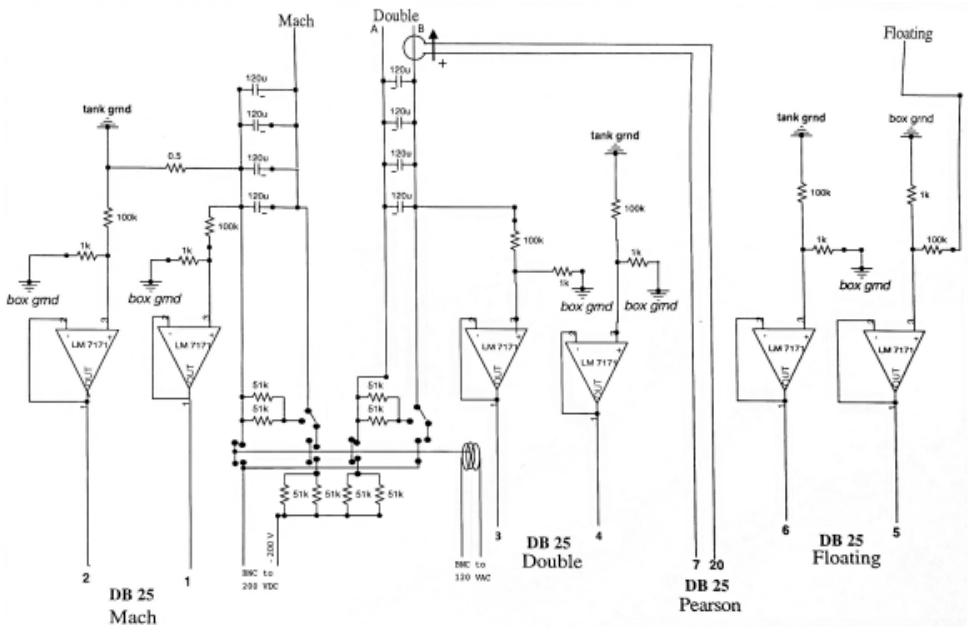

Figure 3.2: Original circuit layout for the quadruple Langmuir probe with the use of unity gain buffer op-amps. The use of repeated grounds is to eliminate any possible ground loops. The two, three-way switches are a safety measure, creating a resistive dump circuit for the capacitors so they do not remain charged after the HVPS is turned off since the entire box is floating.

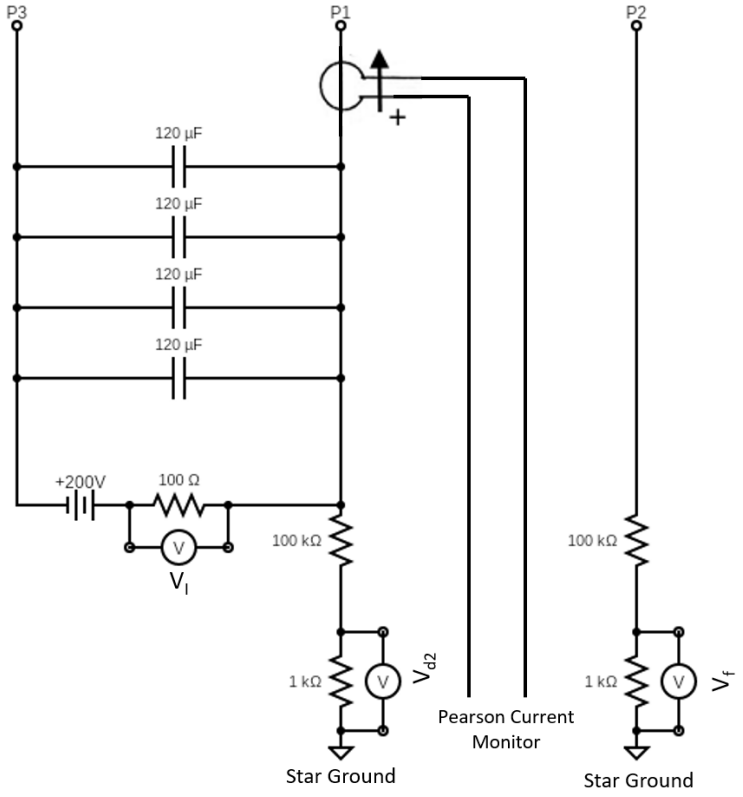

Figure 3.3: The redesigned and simplified Langmuir probe circuit. P1 and P3 are the double probe and correlated to the numbering shown in Fig. 2.3. The current was measured in two ways. V_I measured a voltage drop and used Ohm's law to calculate the current. A Pearson current monitor was also used and deemed more accurate as it is not as susceptible to EMI. V_{d2} and V_f are measuring the double probe voltage and floating voltage respectively. Both circuits where grounded to the lab star ground to eliminate ground loops.

matching for the various probe tips. The double voltage measurement is a high impedance measurement and thus needs to have a 1MΩ input impedance into the scope. In contrast, the floating voltage measurement is set to an input impedance of 50 Ω to reduce the ringing in the signal. The double probe current is measured via a Pearson Model 2878 current monitor probe and needs an input impedance of 1MΩ as well per its instructions.

The double probe is biased to 200 V by a DC high voltage power supply (HVPS). This power supply is floated to eliminate any ground loops. To prevent charge buildup, the casing of the power supply is routed to star ground of the experiment through an alligator clip. During a pulse, the scope was triggered 2 ms before experiment time zero and collected one million data points over a 4 ms timespan. This gave data sampled at 250 MS/s. This window and rate were chosen for two main reasons. Triggering the scope 2 ms before the machine was fired gives zero-offset values for each input and mitigates any noise introduced into the cables from the machine firing. Collecting data for 2 ms during the pulse ensures the entire pulse is captured and gives a data collection rate that does not oversample the signal and capture unwanted noise. When lowering a sample rate, one must ensure the Nyquist criterion is still met. The Nyquist criterion states that the sampling frequency be at least twice the highest frequency contained in the signal [11]. It is difficult to know the exact highest frequency the triple probe will see. From preliminary density measurements, the plasma frequency is approximately 90 GHz. This would require a sampling rate of 180 GHz to realize plasma property changes at the plasma frequency. This is not feasible with the oscilloscope used and EMI present. The sampling rate chosen gives the ability to reconstruct plasma property changes at 125 MHz. The most probable highest frequency change in plasma properties is on the order of the pulse lifetime of a megahertz. Using this assumption, the Nyquist criteria is satisfied. The data from each shot was saved to a local USB drive and transferred to the analysis computer later.

As discussed earlier, the probe is mounted on a translation stage to allow varying the radial location of the probe in the plume. This stage allows the probe tip to be positioned at the machine axis (r=0 mm) or at the far extent of the outer electrode (r=100 mm).

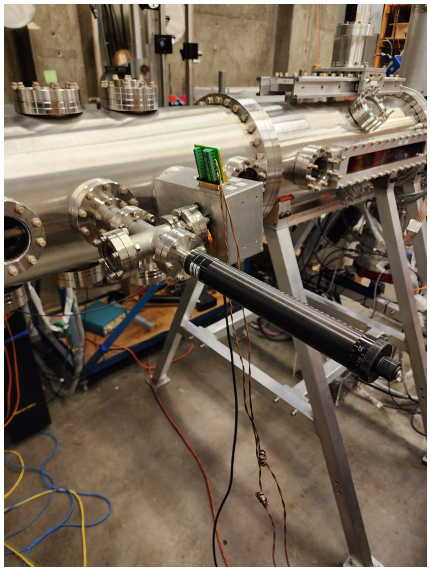

(a) Triple Langmuir Probe attached to the vacuum extension vessel of ZaP-HD. The translation stage is the long black cylinder with the electronics box coming off of the four way nipple.

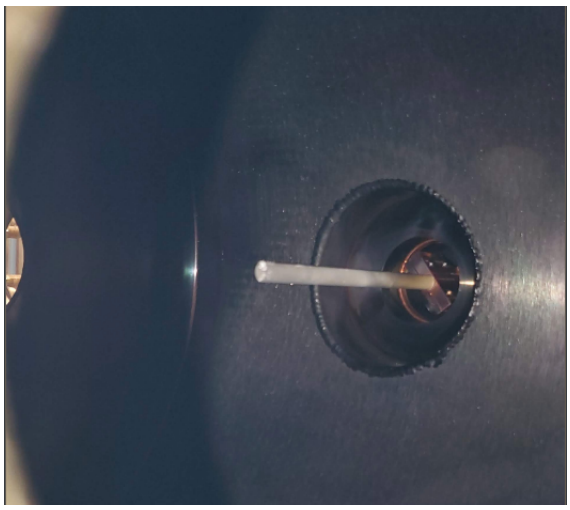

(b) The triple Langmuir probe on the inside of the vacuum chamber. The part that is most prevalent is the alumina housing

Figure 3.4: Lab setup of the Langmuir probe, both an external and internal view. In Fig.3.4a the translation stage and electronics box are visible.

Additionally, there are numerous conflats on the vacuum extension on which the probe can be mounted. Fig. 3.4a shows how the probe is mounted to the side of the vacuum extension and Fig. 3.4b shows how the probe itself is positioned in the vacuum extension. Only the first two conflats were used due to the plasma being too diffuse and signals on the triple probe were negligible by the third conflat. For each z-axis location, the probe measured from the machine axis to r=80 mm in steps of 5 mm. This was chosen as it gave decent spatial resolution of radial trends in the plasma parameters without producing excessive experiment time.

3.2 Ion Doppler Spectroscopy Setup

IDS is a native diagnostic on ZaP-HD and thus did not require any additional modification or repairs. The system consists of a telecentric telescope, a split fiber bundle of ten fibers each, a SP-556 spectrometer (0.5 meter focal length, 3 grating turret), and a Pi-Max 4 P43 ICCD camera. The telecentric telescope is used to ensure there are no errors due to parallax. This is needed because it is difficult to know if the center of the plasma aligns with the center of the machine. There are 10 chords spaced linearly apart by 2 mm on each of the two fiber heads. The line of chords is oriented perpendicular to the machine axis. This orientation enables some spatial variances in emitted light to be collected. The spectrometer has three different diffraction gratings that can be used: 3600 g/mm, 2400 g/mm, 150 g/mm. The unit, g/mm, is referencing how many grooves per millimeter there are on the diffraction grating. The higher g/mm allows for better resolution of spectra at the expense of a smaller field of view. The Pi-Max has a resolution of 1024x1024, this means that at higher g/mm each pixel corresponds to a small fraction of a wavelength. Light Field software was used to capture the image of the spectra from the ICCD camera. The spectrometer was not able to be controlled through Light Field due to it being an older model. Therefore, a manual wavelength calibration was done. A cadmium pen lamp was used as a calibration source. This was advantageous due to the Cd I and Cd II lines that show up near the C III line of interest in the plasma, Fig. 3.5. A linear relationship between pixel space and wavelength space, Eq. (3.1), was then fit from this spectral calibration data. The C III emission line at 229.687 nm was chosen based on the known relative abundance of carbon that is introduced into the plasma through erosion of the graphite nose cone. In addition, a mixture of methane gas and hydrogen can be fed to the machine to increase the abundance and therefore the relative intensity of the carbon emission lines if needed. This was done for IDS data when the end wall was on due to the relatively lower abundance of plasma that makes it through the exhaust hole.

$$\lambda_{actual} = m\lambda_{obs} + b \tag{3.1}$$

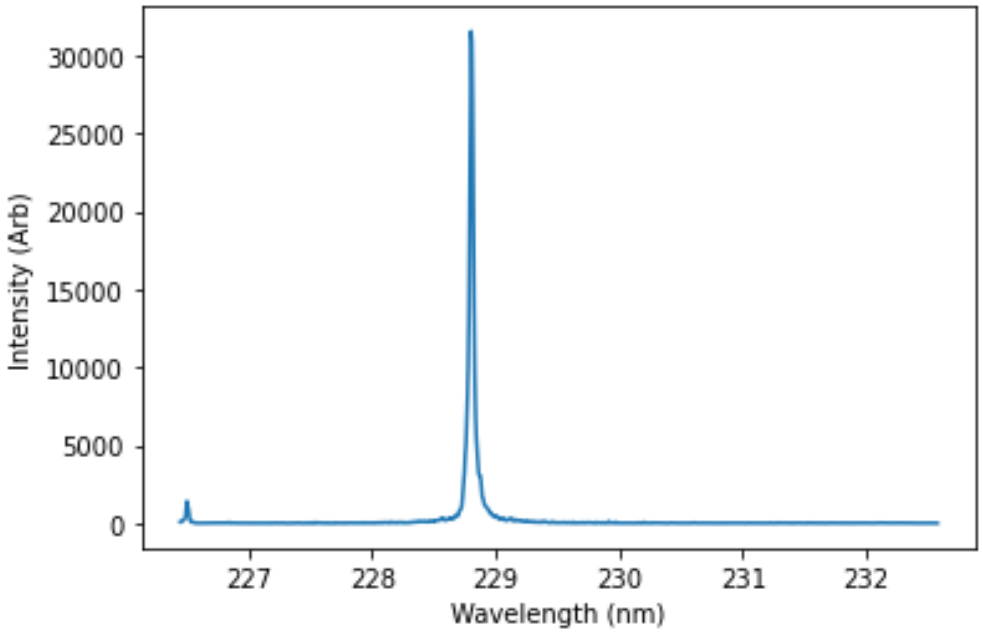

Figure 3.5: Calibration wavelengths utilizing the Cd II 226.5 nm and Cd I 228.8 nm spectral lines. These are located close to the C III 229.687 nm spectral line and are used to make a linear equation to map pixel space to wavelength space.

3.3 End Wall Electrode Configurations

The original configuration of ZaP-HD used a solid 304 SS tungsten-sprayed end wall electrode with an 0.8 inch diameter hole in the center, Fig. 3.7. This geometry resulted in a very constrictive six percent flow through ratio. Any plasma in the pinch itself would be allowed to exit into the vacuum chamber through the central hole. The faster moving sheared-flow plasma around the pinch would be reflected off the end wall and not contribute to the thrust of ZaP-HD. The second configuration that is tested removed the end wall electrode entirely. This was done to remove any obstructions to the plasma and allow all of the mass to be expelled through the end of the electrode at full speed, Fig. 3.8, giving a flow through percentage of 100.

Based on data from Ref. [10, 15] and preliminary results from this paper's research, a trend toward better thruster performance when the plasma had a larger flow through area was apparent. It was also noted that the pinch current and stability decreased when no end wall electrode was present. Additionally, severe arcing from the outer electrode of ZaP-HD to the vacuum chamber or other electrodes was observed. This is detrimental to the longevity of the experiment. This indicates that a single attachment point for the plasma should be defined. This necessitated the design of an end electrode that provides a large flow through area to maximize thrust parameters while including a center hub for the plasma to attach to, providing a single path for current. A new spoked end wall electrode was created to meet this requirement, Fig. 3.9. The material for this spoked design was chosen to be TTK-4 graphite instead of 304 SS with a tungsten spray. Graphite is easier to machine that 304 SS, does not require a tungsten spray and at high temperatures graphite is an excellent conductor. Graphite is, however, substantially weaker than 304 SS, only having one third the flexure strength. A thorough force and structural analysis is done to ensure the new spoked design

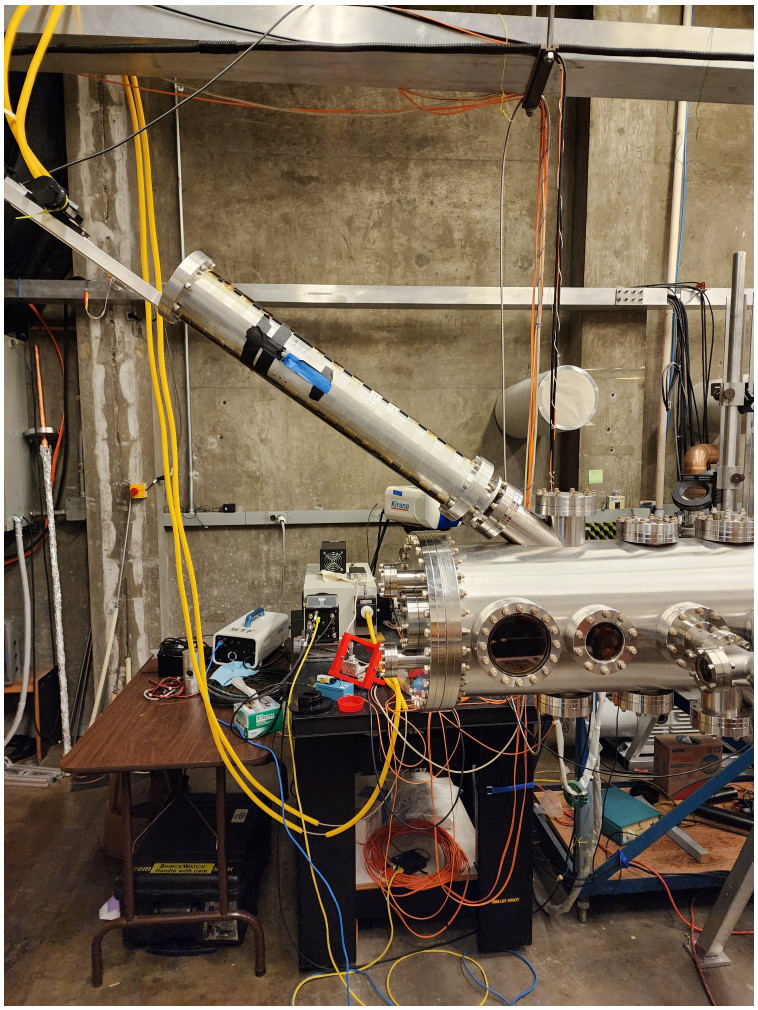

Figure 3.6: Lab set up for ion Doppler Spectroscopy. The oblique telecentric telescope is mounted at a 35 degree angle to machine axis on the vacuum extension vessel. The fiber optics are routed to the spectrometer in yellow sleeving to protect them.

will not fail under operating conditions.

$$F = -\int_V \nabla \cdot \overleftrightarrow{\mathrm{T}} dV \tag{3.2}$$

Eq.(3.2) states that the force applied during operation comes from the divergence of Maxwell's stress tensor, $\overleftrightarrow{\mathrm{T}}$ which is given by,

$$\overleftrightarrow{\mathrm{T}} = -\frac{\vec{B}\vec{B}}{\mu_0} + \left(p + \frac{B_0^2}{2\mu_0}\right) \overleftrightarrow{\mathrm{I}} \tag{3.3}$$

By applying the divergence theorem and applying geometric symmetries at the end wall electrode of ZaP-HD and using jump conditions at the plasma boundary,

$$\left[\!\left[p + \frac{B^2}{2\mu_0} \right]\!\right] = 0 \tag{3.4}$$

a final equation for the force on the end wall electrode is derived,

$$\vec{F} = -\hat{z}\left[\frac{\mu_0 I^2}{8\pi}\left(\frac{3}{2} + 2\ln\frac{b}{a}\right)\right]. \tag{3.5}$$

Eq. (3.5) only has dependence on the current applied, I, the pinch diameter, a and the end wall electrode diameter b. The equation of force takes into account both plasma pressure and magnetic pressure terms. The 3/2 term represents the plasma pressure and is only dependent on the current being pushed through the plasma. This is a relatively small force compared to the force of the magnetic pressure which is the dominant logarithmic term. At peak performance, ZaP-HD can push currents of 300 kA creating a pinch size of 3 mm. The end wall electrode is 95 mm in diameter. These machine parameters yield of a force of 38 kN. The lifetime of a pulse is on the order of 100 μs, so a transient analysis of the resulting force was completed to determine the overall thickness of the spoked electrode. The width of each spoke was determined by the Rogowski coil slots on the rear of the end wall. An iterative process of thickness variation using Ansys Mechanical transient structural analysis determined an overall thickness of 2.6 inches provided a factor of safety of 2.6 in flexure, Fig. 3.10.

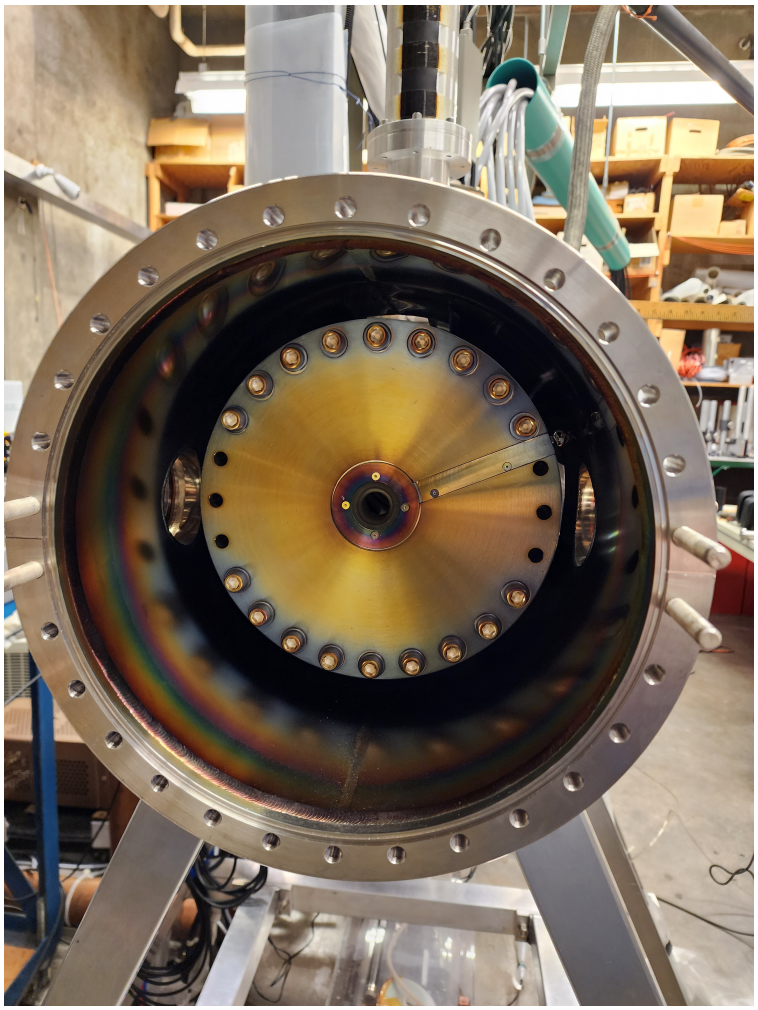

Figure 3.7: Original configuration of ZaP-HD looking directly upstream when the vacuum extension is removed. It is made of 304 SS with a tungsten spray on the plasma facing side. It has a flow through percentage of 6%.

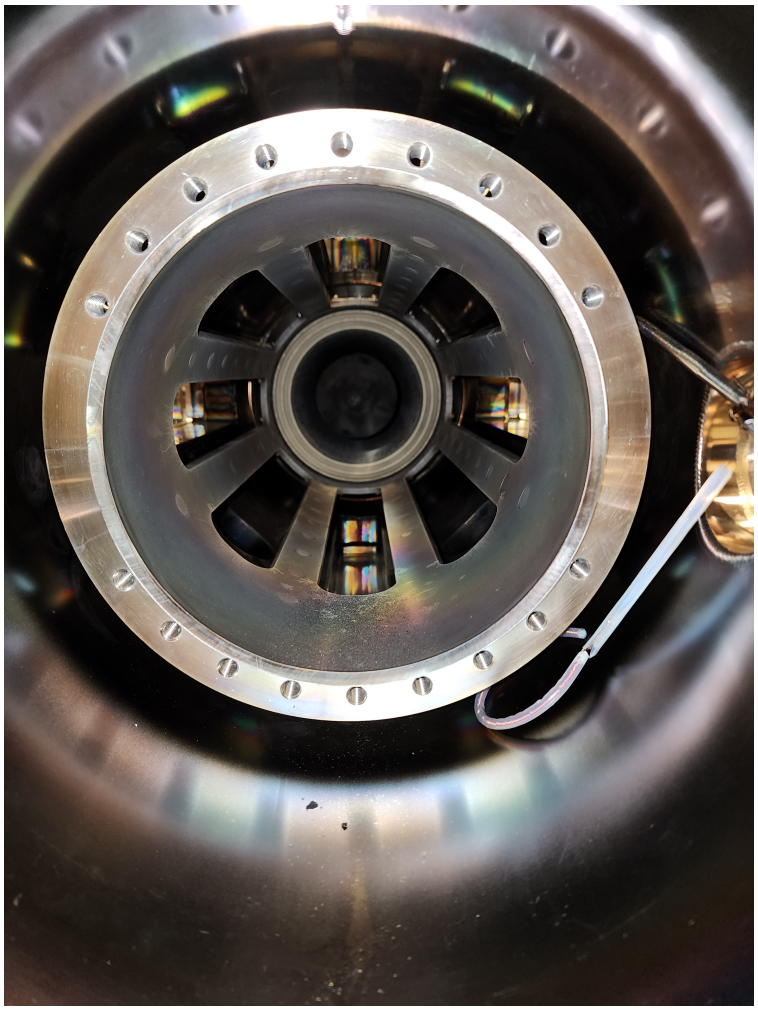

Figure 3.8: Looking upstream of ZaP-HD with the end wall electrode removed. The slots in the outer electrode are to allow the diagnostics to visually access the plasma. The nose cone of the inner electrode can be seen in the center of the picture.

Figure 3.9: The four spoked end wall electrode attached to the outer electrode of ZaP-HD prior to initial testing. This configuration will allow a flow through percentage of 55% while providing an attachment point for the plasma.

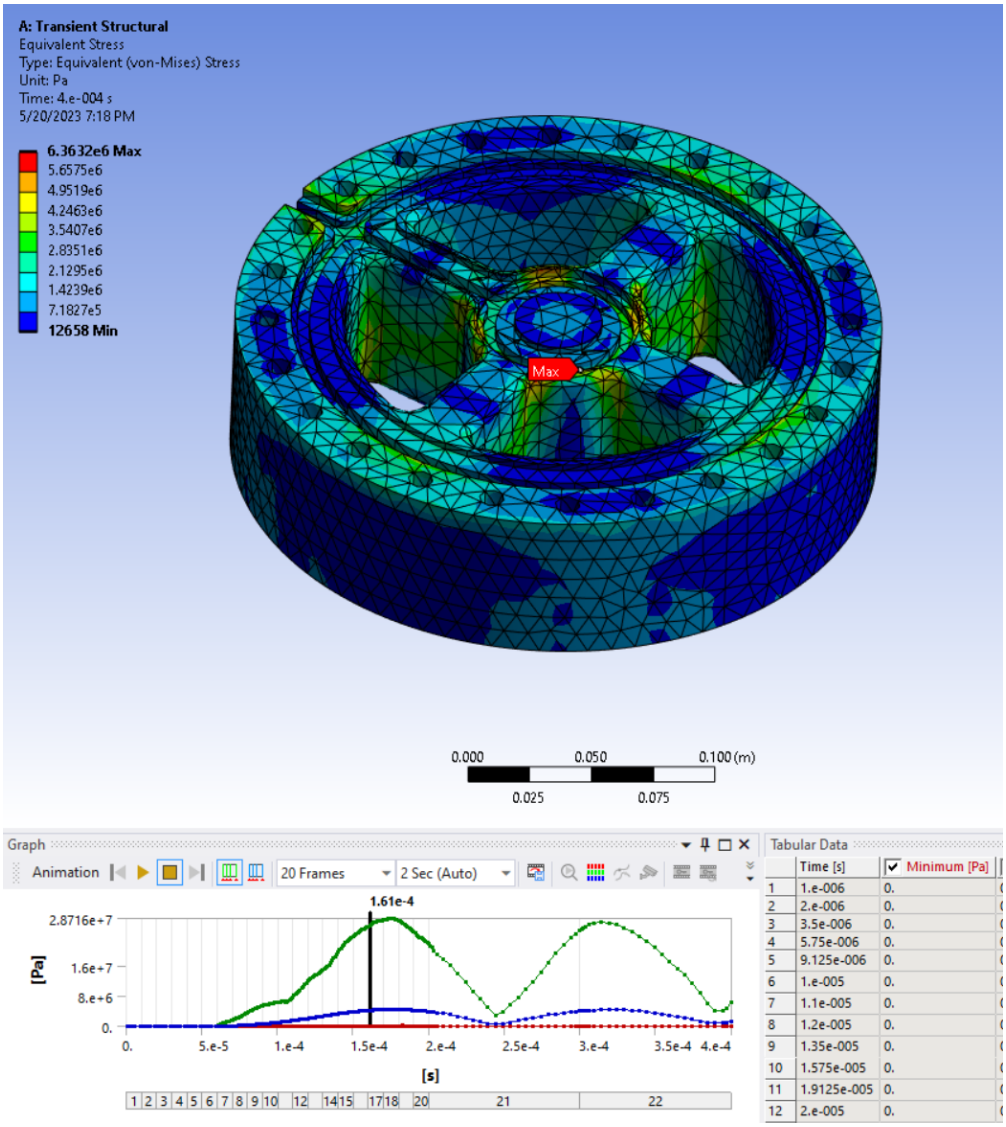

Figure 3.10: Ansys Mechanical transient structural analysis results. The maximum equivalent stress seen is 28 MPa, well below the 73 MPa limit of TTK-4 graphite used. The green trace shows the maximum stress seen by any one element, the blue showing the average with red being the minimum.

Chapter 4
EXPERIMENTAL RESULTS

Determination of plume and thruster characteristics was done by collecting five shots of Langmuir probe data at each radial location for two z-axis locations. This was repeated for all three configurations. Machine operating parameters were chosen as 7 kV acceleration and 5 kV compression. This was chosen as it gave sufficiently high probe signals without causing double probe arcs, which will be discussed later. All but ten pulses were taken with 100% hydrogen gas. The ten pulses in question were taken with 50% methane and 50% hydrogen. This was done to increase the carbon impurity concentration for IDS. This chapter will analyze the overall plume and thruster characteristics found through the culmination of this data.

4.1 Pinch Performance

The concept for a future fusion propulsion device means that not only does thruster performance need to be maximized, but also balanced with pinch performance. It may be possible to have very high thrust performance with an unstable pinch. To this end, it is important to ensure that pinch stability is unaffected or, at a minimum, only slightly changed. The metrics for this are the examinations of the magnetic field at various axial locations, current drive, and the normalized m=1 stability limit of being less than 0.2. The current traces between the configurations are closely comparable. The total plasma current and acceleration currents are the same. This is not surprising as the fundamental physics that drive the acceleration current should be unaltered by the geometry of the end wall electrode. The compression current is the only trace that shows any evidence of a diminished current being driven during compression time in the assembly region. This may be cause of concern, as

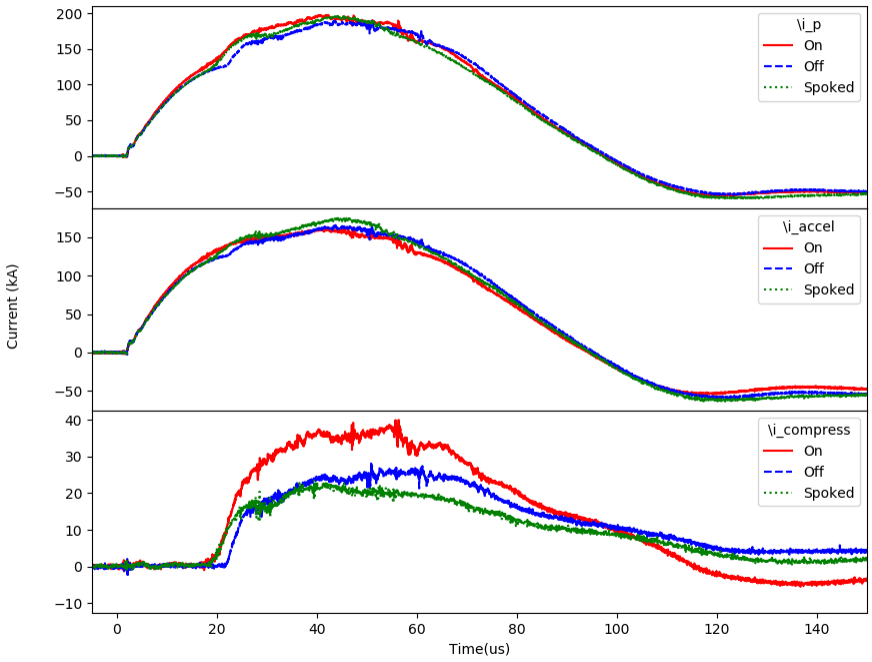

Figure 4.1: Plasma, acceleration and compression current traces for the end wall electrode on: 230110010-230110014, removed: 230407008-230407012 and spoked: 230522020-230522025. There are no appreciable differences from the two configurations other than in the compression current, which is most likely due to a faulty Rogowski coil.

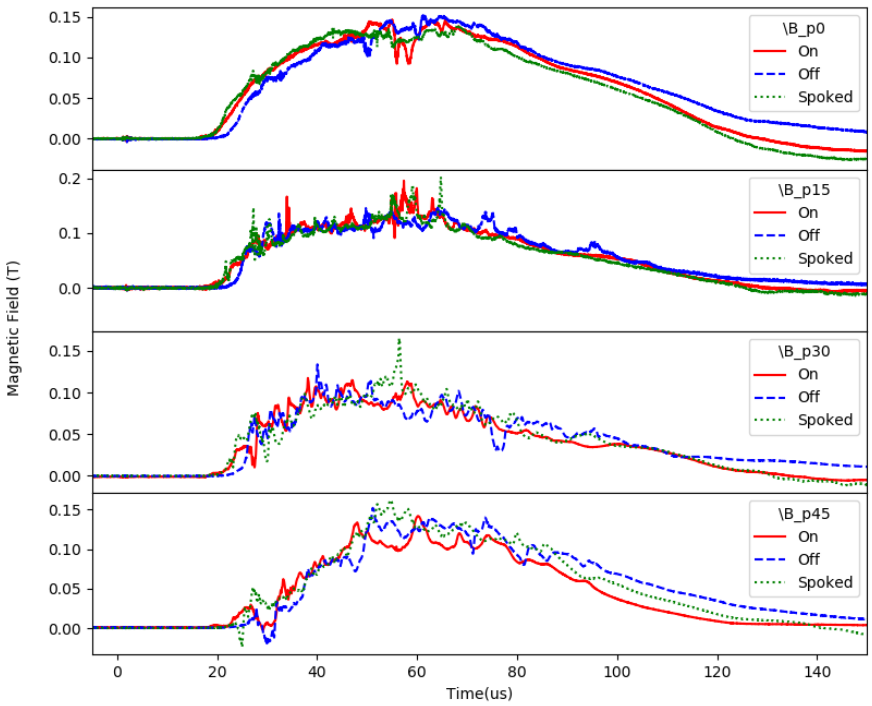

Figure 4.2: Magnetic field trace comparison for the two end wall electrode configurations, on: 230110010-230110014, removed: 230407008-230407012 and spoked: 230522020-230522025. The magnetic field traces are not appreciably different, implying similar pinch performance.

this would result in less current being driven through the pinch and thus reduce plasma parameters to create fusion conditions in a full scale thruster. However, there are a few different reasons for this discrepancy other than the geometry change. The primary culprit is that the Rogowski coil measuring the compression current has been called out as possibly being faulty. This concern arises from the acceleration and compression current not adding up to the total plasma current as it should. Another possibility comes from examining the magnetic field data, Fig. 4.2. From these plots, it is apparent that the magnetic field magnitudes are independent of an end wall electrode configuration. The only notable difference are the tails of these traces, namely at the P45 location. Because the magnetic field is higher

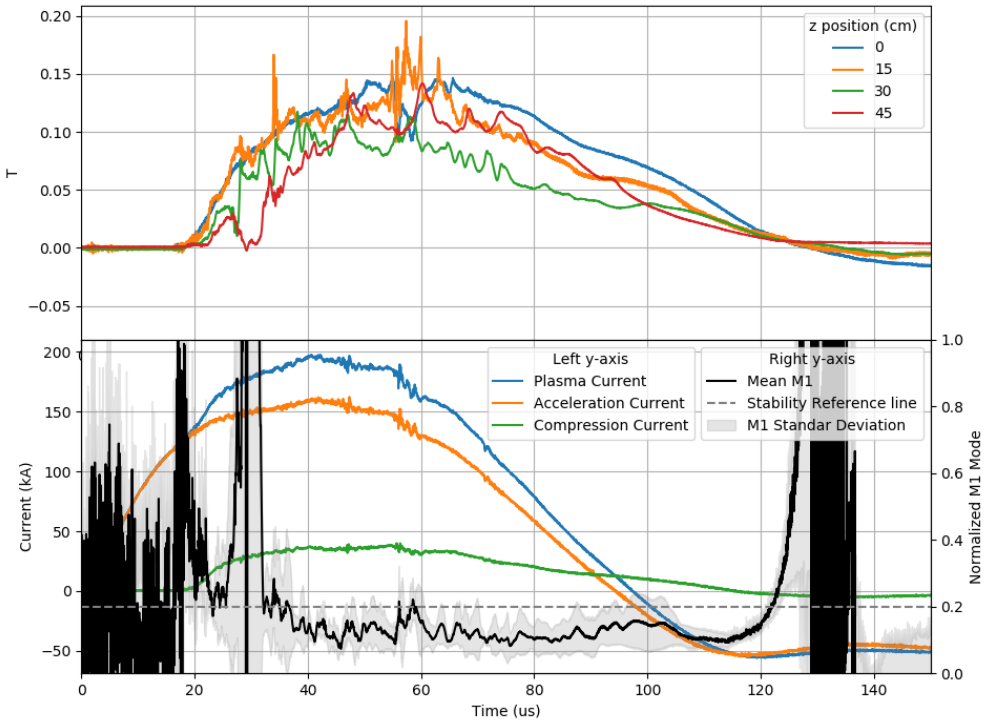

Figure 4.3: Normalized $m = 1$ stability plotted in time with magnetic field and current traces for the end wall electrode attached for shots: 230110010-230110014. This configuration demonstrates acceptable stability during peak current time.

late in time does not have any negative impacts to the pinch. What the magnetic fields being comparable does imply, is that the total current through an Amperian loop must be the same between the configurations. This gives supporting evidence that the compression Rogowski coil is not measuring accurate values and that the total current being pushed during the compression time is the same between electrode configurations. The similarities, thus far, is continued when looking at the stability of the pinch, Fig. 4.3,4.4,4.5.

The magnetic field and current trace data are duplicated here to enable correlations with various stability events to current and magnetic field phenomenon. The normalized mean m=1 mode corresponds to how well the current is centered in the machine. A normalized value of 0.2 indicates that the current is within 2 cm of the center of the machine axis.

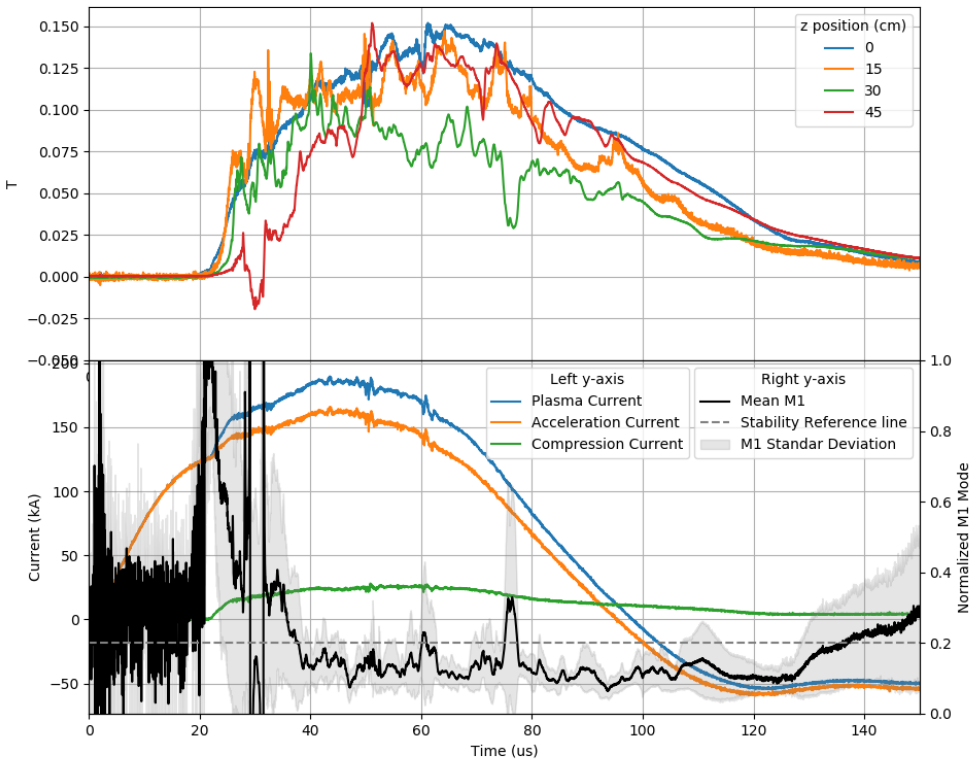

Figure 4.4: Normalized $m = 1$ stability plotted in time with magnetic field and current traces for the end wall electrode removed for shots: 230407008-230407012. This configuration shows acceptable stability during peak current time, but appears to become more unstable as the current falls; resulting in a shorter quiescent period.

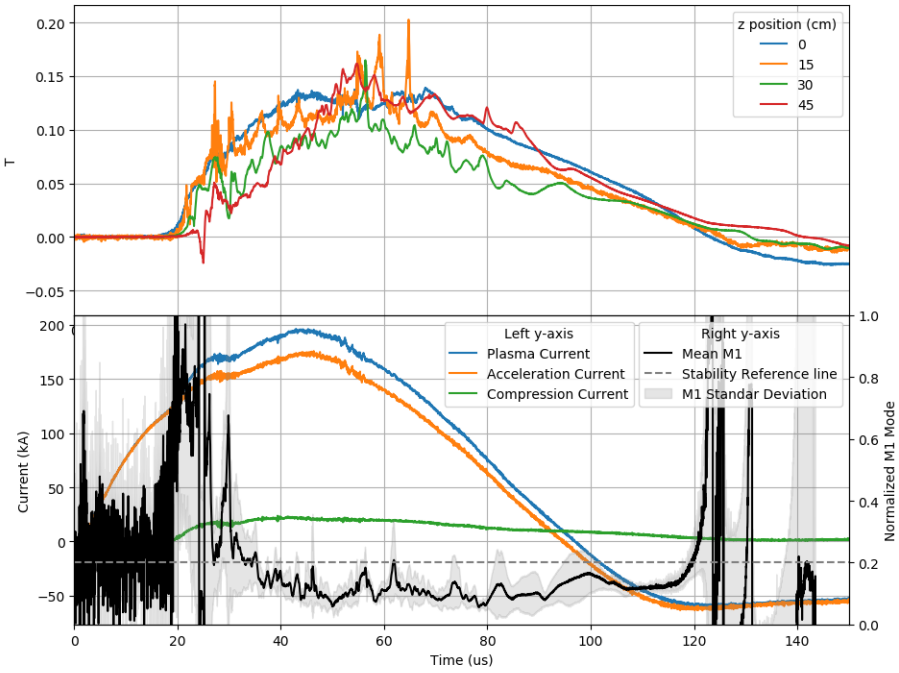

Figure 4.5: Normalized $m = 1$ stability plotted in time with magnetic field and current traces for the spoked end wall for shots: 230522020-230522025. The spoked end wall shows acceptable stability across the entirety of the current wave form.

Any displacement larger than this is considered unstable. The main difference between the stability of the electrode configurations is the time and abruptness of when the quiescent period ends. The quiescent period is defined as the time when the m=1 mode is below the 0.2 threshold value. The end wall electrode being on creates a much more violent current center disruption than the end wall electrode being off. This is in part due to the extended elevated magnetic field seen in the open configuration. The m=1 mode is normalized to the m=0 mode which creates an asymptote for the m=1 mode as m=0 goes through zero. This can be seen happening around 130 micro-seconds in Fig. 4.4. This also corresponds well with the magnetic field dropping to zero, which indicates the end of any plasma. Based on the standard deviation of the m=1 mode, the end wall electrode being present does seem to increase the stability margin. This is further supported by examining the stability of the spoked end wall. The standard deviation reflects more on how stable the pinch is during its lifetime. The $m = 1$ data shown is averaged over multiple axial locations in addition to multiple shots. A higher standard deviation could be caused by two different events. Either the shot-to-shot stability of the pinch is very different, or the axial stability along the the pinch is different for a given shot. A more detailed shot-to-shot look at the $m = 1$ stability would need to be examined to separate these effects. Nevertheless, the overall stability matches that of the original end wall, with increased stability around 60 μs. The more restrictive end wall will reflect plasma and create a reversing in the sheared flow direction. During this reversal, the pinch is more susceptible to instabilities. The spoked end wall allows most of the plasma to be exhausted into the vacuum extension and not be reflected. The flow reversal is now minimized creating a more stable pinch.

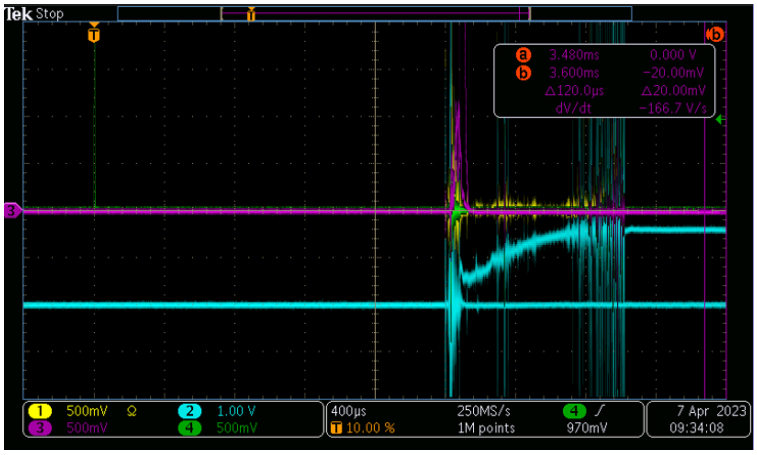

Figure 4.6: Example of raw Langmuir Probe data. The blue signal is the double probe voltage, yellow is the floating voltage, purple is the voltage reading from the Pearson current monitor, and green is the trigger to the scope. The double probe voltage that returns to its pre-shot value is not an arc. The other trace shows when an arc happens between the double probe tips.

4.2 Langmuir Probe Results

A total of 200 shots were taken with the Langmuir probe. Positions varied from the machine axis (r=0 mm) to near the extent of the outer electrode (r=80 mm) in steps of 5 mm. This was completed for the two closest conflats/flanges on the vacuum extension. These correspond to 267 mm and 435 mm from the exit plane of the end wall. Each spatial position required at least five shots for statistical significance. All plots that follow have been averaged over these five pulses. This method also aids in averaging out any noise. The raw data produced by the oscilloscope was noisy as expected. In Fig. 4.6, there are two shots laid over one another. The double probe voltage that does not return to its pre-shot value is due to an arc forming between the double probe tips as discussed in Ref. [15]. This creates non-physical results in the analysis so these data sets were discarded. The post processing of the data included an averaging over five shots then using an exponential weighted function window to smooth the data. These signals could then be used to calculate

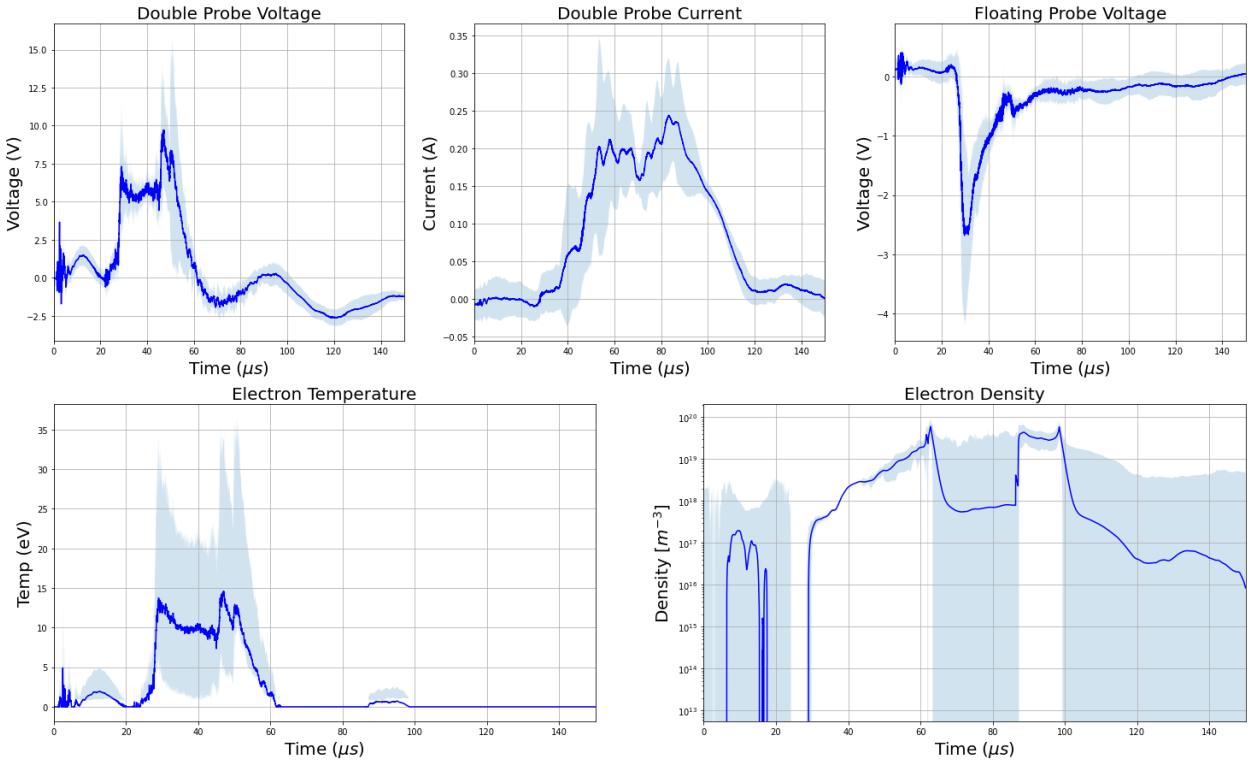

Figure 4.7: Plasma parameters of electron temperature and density along with the triple Langmuir Probe signals for $z = 267$ mm and $r = 0$ mm with the end wall electrode on.

electron temperature and density. The output of this algorithm can be seen in Fig. 4.7. The electron density was plotted using a log scale on the y axis to better illustrate when density is present, as the large magnitude differences over time tended to hide the early onset of density. The electron density plot is also the most irregular, meaning large standard deviations and rapid fluctuations. This is the case for the majority of the locations and is not an outlier for the specific position shown. This is due largely in part to the electron density equation sensitivities noted in the theory section. To ensure only physical results were analyzed, an I-V characteristic was reconstructed, Fig. 4.8 for any time there may be interesting physics occurring in the density trace. A triple probe cannot collect the electron saturation current, hence why it is missing from the reconstruction. This is not of consequence as the electron

saturation current is often difficult to measure even for swept single probes because it is often quite high. The goal of I-V characteristic reconstruction was to verify that the exponential region of the graph corresponded to what one would expect. If the reconstruction yields a step function, the data is considered non-physical. This step function was consistently seen during reconstructions using data after 70 μs. As Fig. 4.8b illustrates, the small electron temperature at this point in time results in a very steep exponential region. It was found that beyond this threshold, the reconstruction yielded a slope of infinity due to a zero electron temperature. From this analysis it was conjectured that this triple probe set up has an electron temperature minimum of an electron volt. Any analysis done henceforth will only focus on data with a corresponding electron temperature greater than an electron volt. This often occurs in the time domain of 0-70 μs.

End Wall Electrode On

The original configuration of ZaP-HD allowed for a full spatial characterization of the plume. While arcing between the double probe tips was seen, it was rare enough to afford getting the needed quantity of data desired. Electron temperatures observed ranged from 15 eV up to 40 eV depending on the exact spatial location. Radial variations in electron temperature and density values are explored in the following chapter. Non-physical measurements happen when the double probe voltage reading rings below zero. This would create a negative electron temperature mathematically. As clearly this is not a real result, these artifacts are discarded and the electron temperature is set to zero. The rather unfortunate consequence of this treatment is creating extremely large uncertainties in electron density during these intervals. As discussed previously, the I-V characteristic reconstruction for these times would yield a step function and would not reflect any real physics. In the following figures any time interval of the density that has standard deviations that reach the x axis are non-physical regions. The standard deviation confidence interval is the shaded region around the signal trace. During high confidence intervals the density is seen to be on the order of 10^{19} m^{-3} for all radial positions. Another interesting result is that the plasma potential is consistently

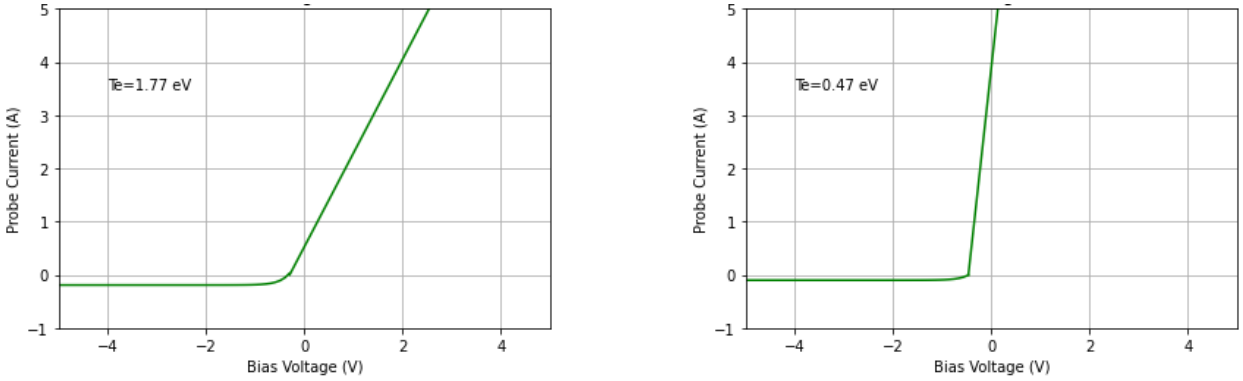

(a) Reconstructed I-V characteristics at t=60 μs from the triple Langmuir probe when positioned at z =267 mm and r=0.

(b) Reconstructed I-V characteristics at t=70 μs from the triple Langmuir probe when positioned at z =435 mm and r=0.

Figure 4.8: Sample Reconstruction of I-V Characteristics from Triple Langmuir Probe.

negative as illustrated by the floating probe voltage trace for each position.

The z=267 position data was also extended to r=100 in an attempt to further investigate the plume divergence for the end wall electrode being installed. It was previously calculated by [10] that the ZaP-HD plume divergence was around 15 degrees. A 15 degree divergence of the plume would intersect the first conflat z-axis at a radial position of 80 mm from machine axis. One would then expect a large drop in electron density beyond this point. Based on when the density was seen to drop most rapidly from $r = 85$ to $r = 95$ the plume divergence would then be 20 ± 4 degrees showing that within error these measurements agree with Ref. [10].

End Wall Electrode Removed

Double probe electrode arcing was rampant during shots with end wall electrode removed. This is not entirely surprising as the Langmuir probe is now directly exposed to the highest density plasma coming from the assembly region. Due to this, it was only feasible to collect shots at the far extent of the outer electron, $r = 100$ mm. Being constricted to one spatial point in the plume negated any ability to build a view of the inner plume characteristics. The

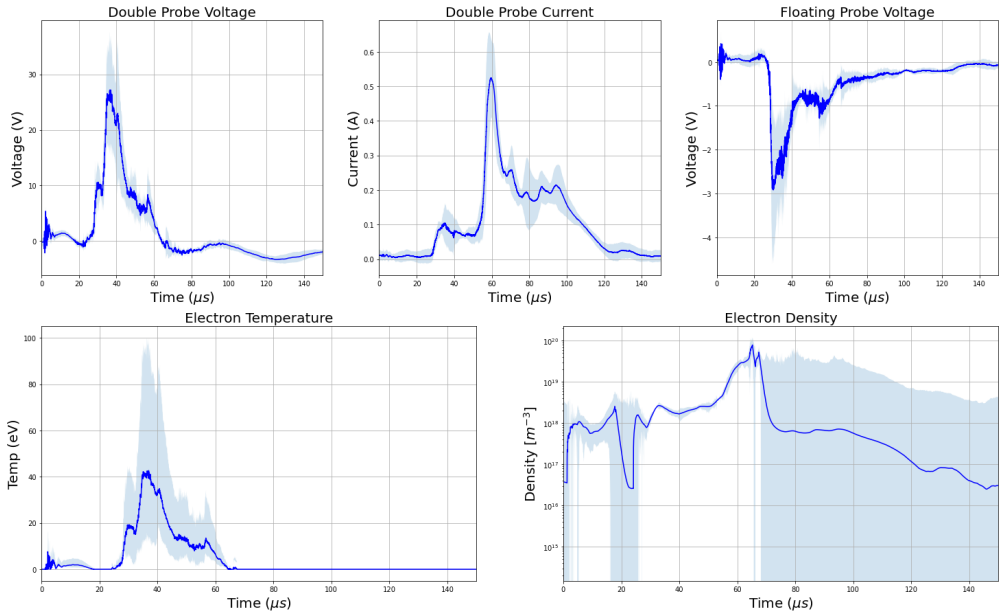

(a) Plasma parameters of electron temperature and density along with the triple Langmuir probe signals for $z = 267$ mm and $r = 20$ mm.

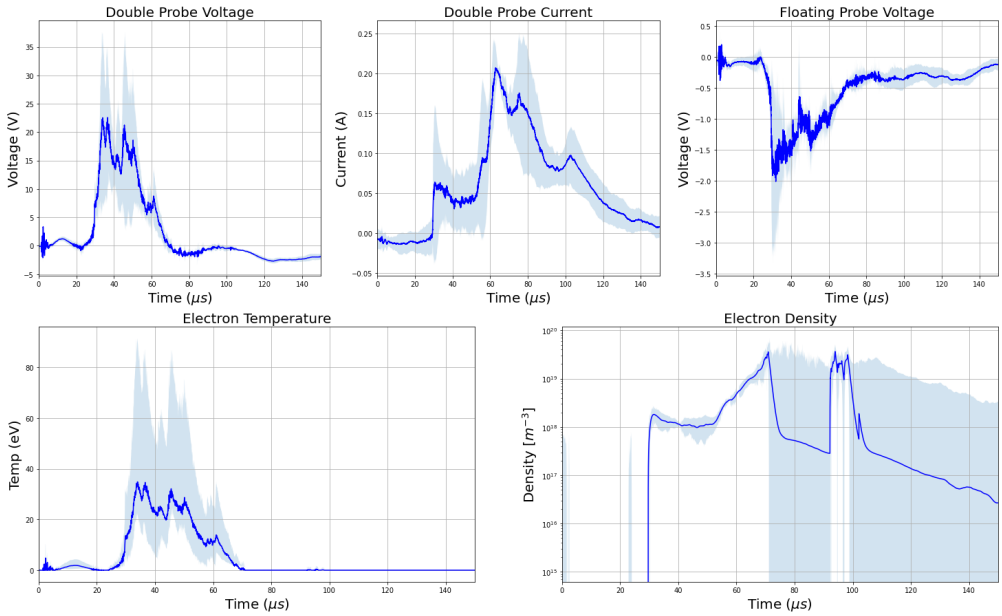

(b) Plasma parameters of electron temperature and density along with the triple Langmuir probe signals for $z = 435$ mm and $r = 20$ mm.

Figure 4.9: Triple Langmuir probe results for $r = 20$ mm at both axial locations with the end wall electrode on. The standard deviations are shown in the shaded region.

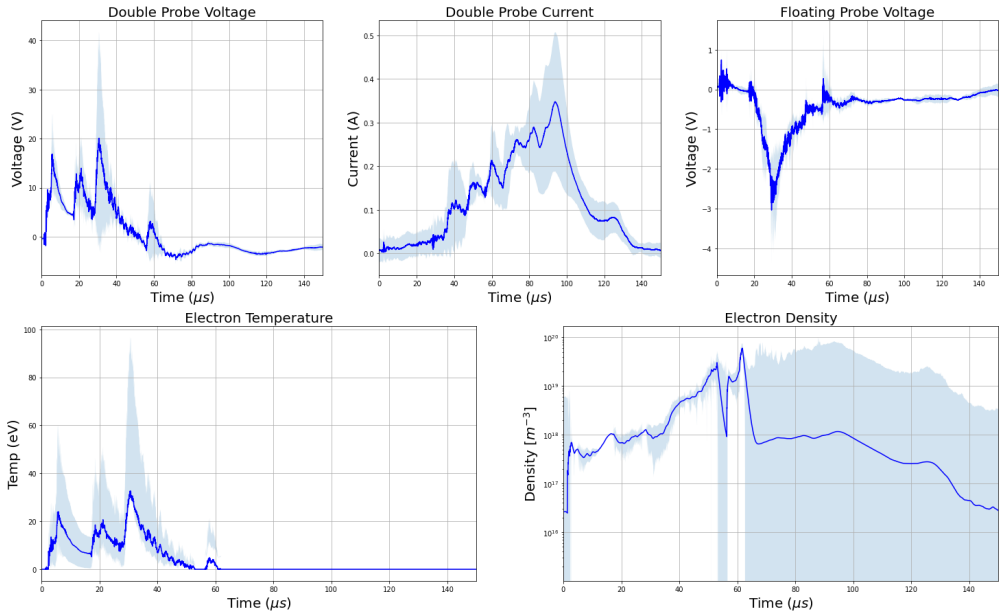

(a) Plasma parameters of electron temperature and density along with the triple Langmuir probe signals for $z = 267$ mm and $r = 40$ mm.

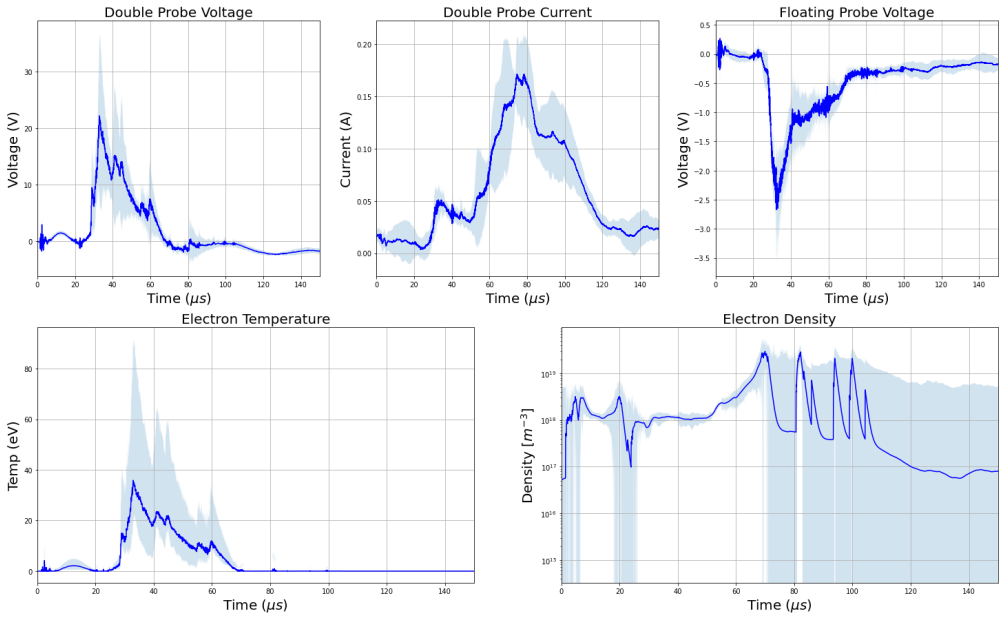

(b) Plasma parameters of electron temperature and density along with the triple Langmuir probe signals for $z = 435$ mm and $r = 40$ mm.

Figure 4.10: Triple Langmuir probe results for $r = 40$ mm at both axial location with the end wall electrode on. The standard deviations are shown in the shaded region.

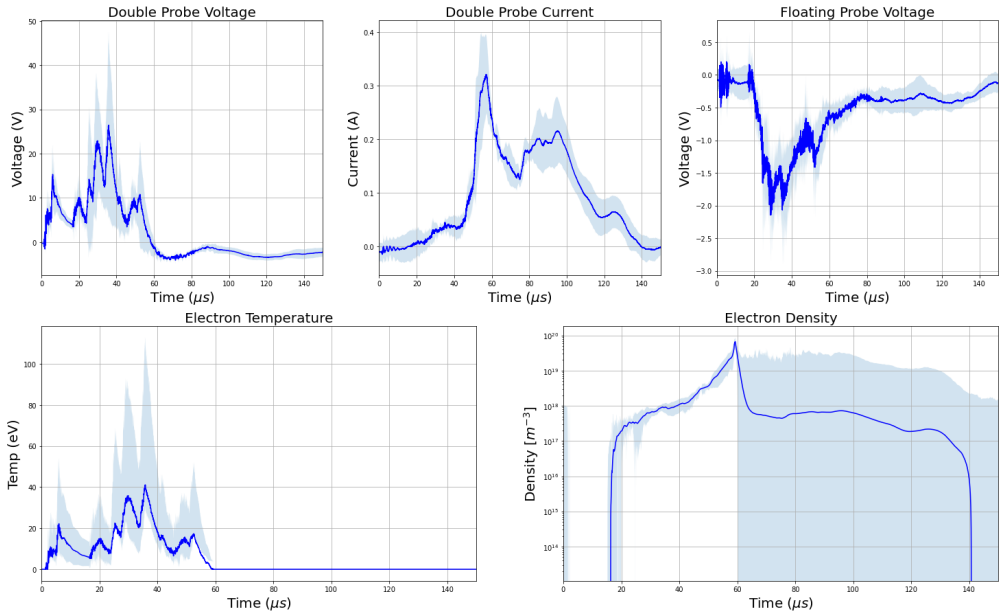

(a) Plasma parameters of electron temperature and density along with the triple Langmuir probe signals for $z = 267$ mm and $r = 60$ mm.

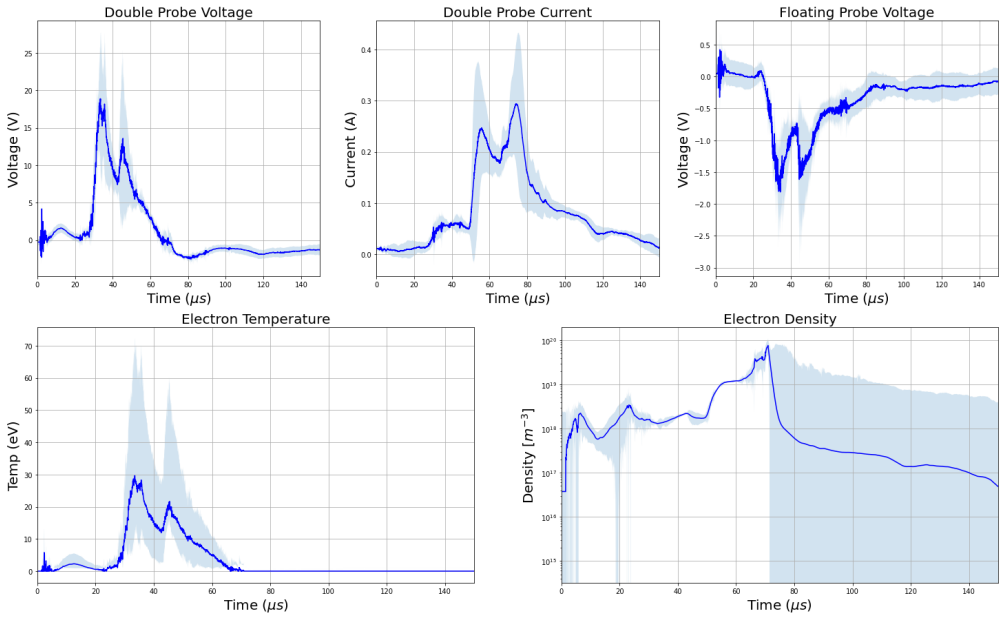

(b) Plasma parameters of electron temperature and density along with the triple Langmuir probe signals for $z = 435$ mm and $r = 60$ mm.

Figure 4.11: Triple Langmuir probe results for $r = 60$ mm at both axial location with the end wall electrode on. The standard deviations are shown in the shaded region.

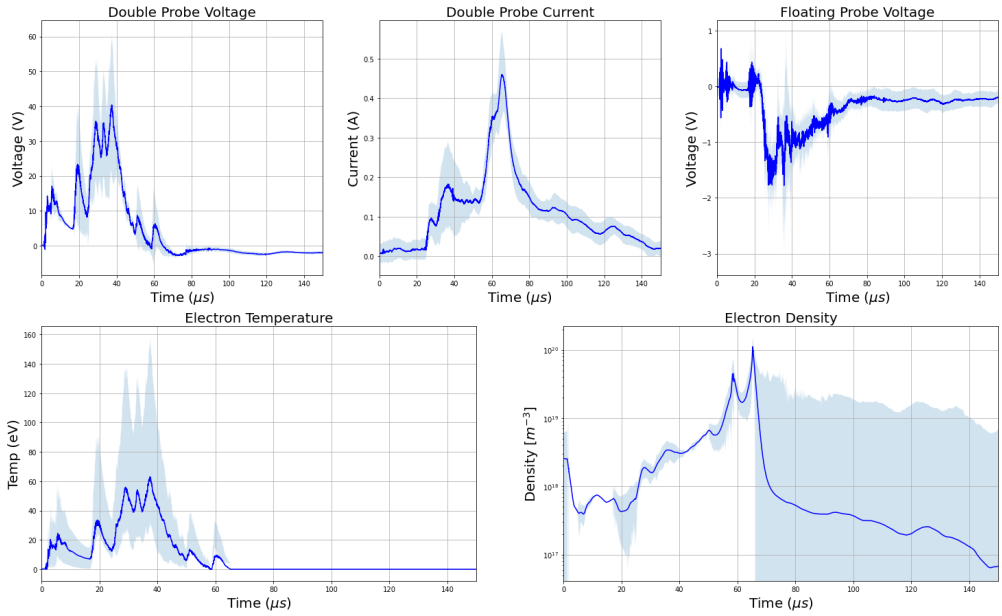

(a) Plasma parameters of electron temperature and density along with the triple Langmuir probe signals for $z = 267$ mm and $r = 80$ mm.

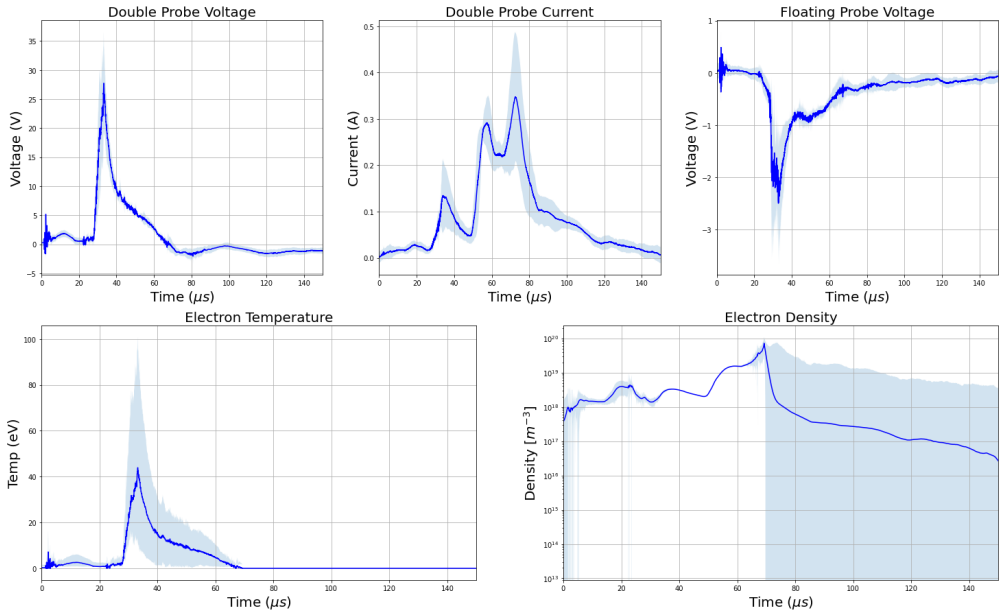

(b) Plasma parameters of electron temperature and density along with the triple Langmuir probe signals for $z = 435$ mm and $r = 80$ mm.

Figure 4.12: Triple Langmuir probe results for $r = 80$ mm at both axial location with the end wall electrode on. The standard deviations are shown in the shaded region.

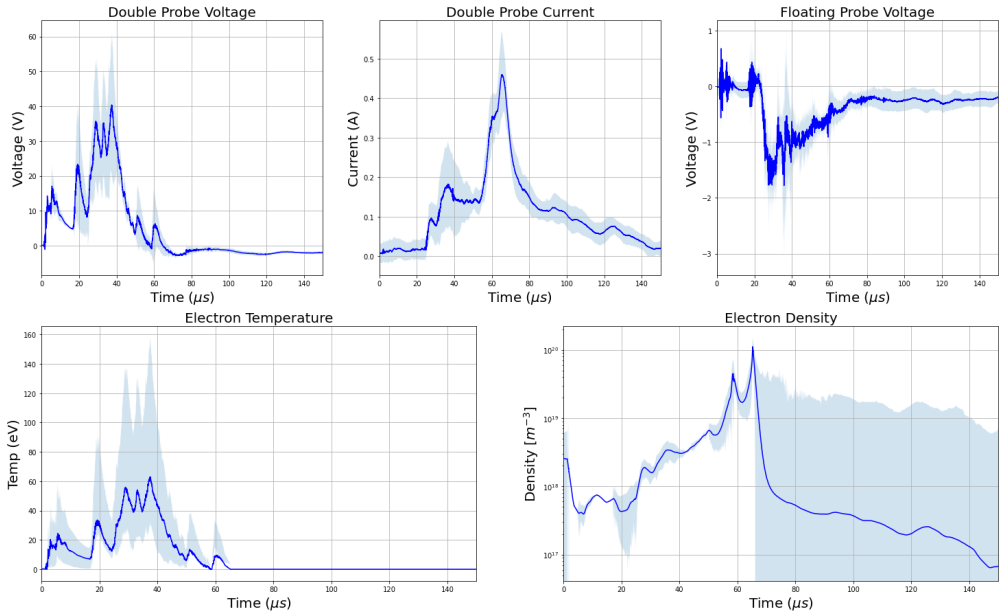

(a) Plasma parameters of electron temperature and density along with the triple Langmuir probe signals for $z = 267$ mm and $r = 80$ mm

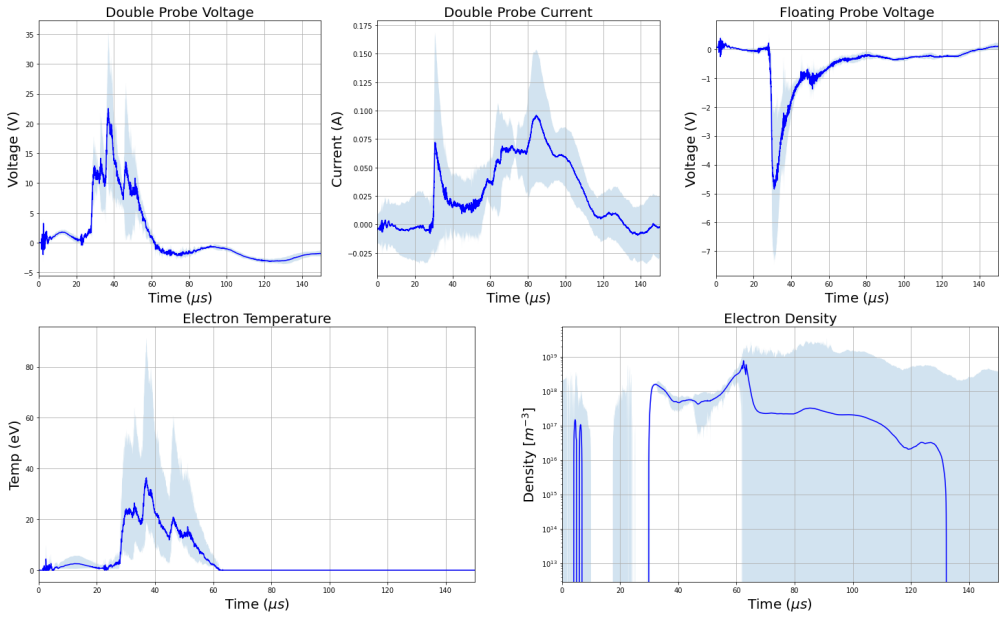

(b) Plasma parameters of electron temperature and density along with the triple Langmuir probe signals for $z = 267$ mm and $r = 90$ mm

Figure 4.13: Comparison of triple Langmuir probe results at $r = 80$ and $r = 90$ at the first axial location with the end wall electrode on.

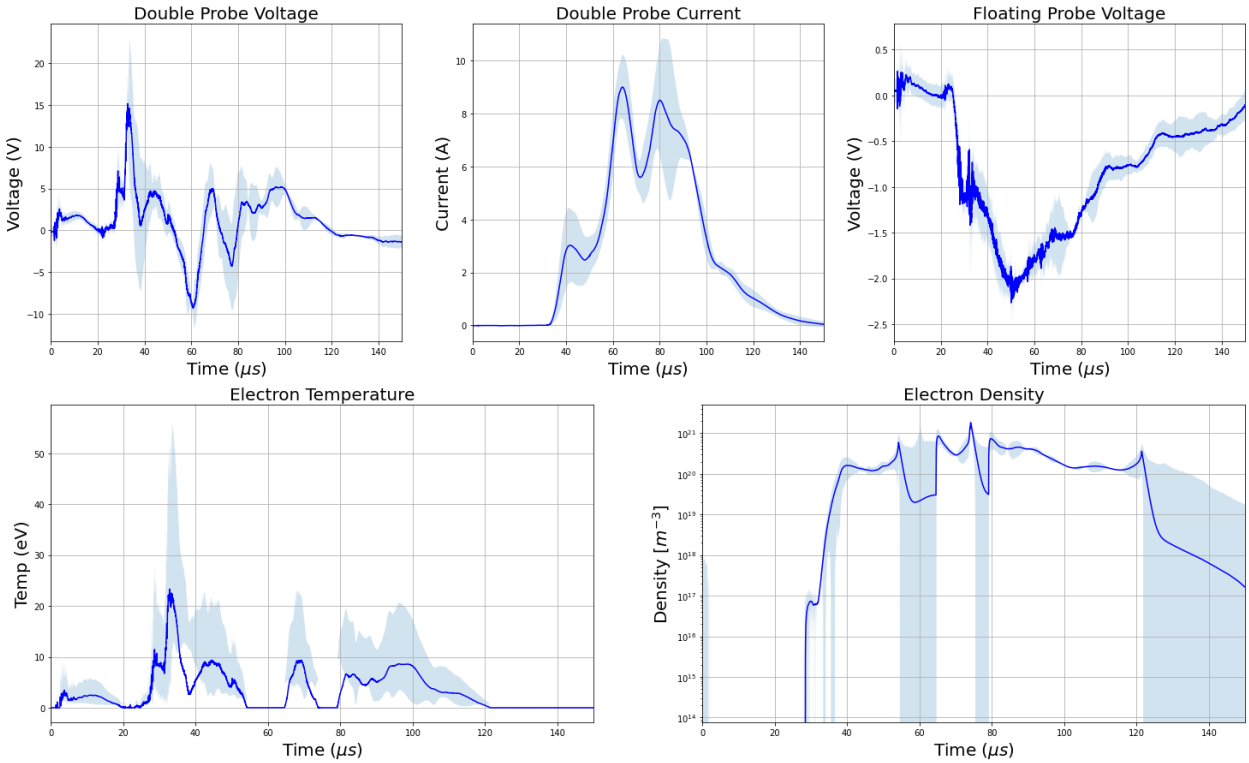

Figure 4.14: Plasma parameters of electron temperature and density along with the triple Langmuir probe signals for $z = 603$ mm and $r = 100$ mm with no end wall electrode.

ensuing calculations of thrust parameters used an assumption that the density was uniform throughout the plume. This assumption was informed by the density characteristics of the other two configurations. Although electron temperatures were not meaningfully higher with this configuration, 20 eV, the electron density did jump an order or magnitude from the end wall being on. The density measurements are now near 10^{21} m^{-3}. Once again only analyzing sections of the density graph where there is corresponding electron temperature. The hypothesis that higher density plasma is now making it to the probe is supported via the increase of the double probe current as well as the jump in electron density to a peak of 10^{21} m^{-3} at 100 mm radius as compared to 10^{18} m^{-3} seen at that same radius, but with the end wall electrode on.

Spoked End Wall

The goal of the spoked end wall was to allow a significant portion of the plasma to be able to flow into the vacuum extension while still providing an attachment point for the plasma. There was still concern of double probe arcing as from $r = 10$ to $r = 60$ the probe is exposed directly to the assembly region plasma. The probe was intentionally oriented such that it would not be in a "spoke shadow." Fortunately, arcing was not an issue with this configuration. The traces in Fig. 4.15 reveal smoothly varying plasma parameters which is in contrast to the rather eradicate behavior seen previously in other configurations. The reduced level of ringing in the double probe voltage creates larger spans of time in the electron density trace that have higher confidence of physical results. It is intriguing that non-negligible electron temperature and density are present at the machine axis. The solid center hub of the spoked end wall would not allow any plasma to in this region. This suggests that there is sufficient divergence in the plume to have a significant plasma presence in this location. The spoked configuration saw a decrease in plasma temperature to 10 eV while still maintaining similar densities as the original end wall: $4*10^{19}$ m^{-3}. The plasma parameters recorded as the probe was retracted show that there is little change in the plasma. The shape and magnitude of the temperature and density profiles remain the same.

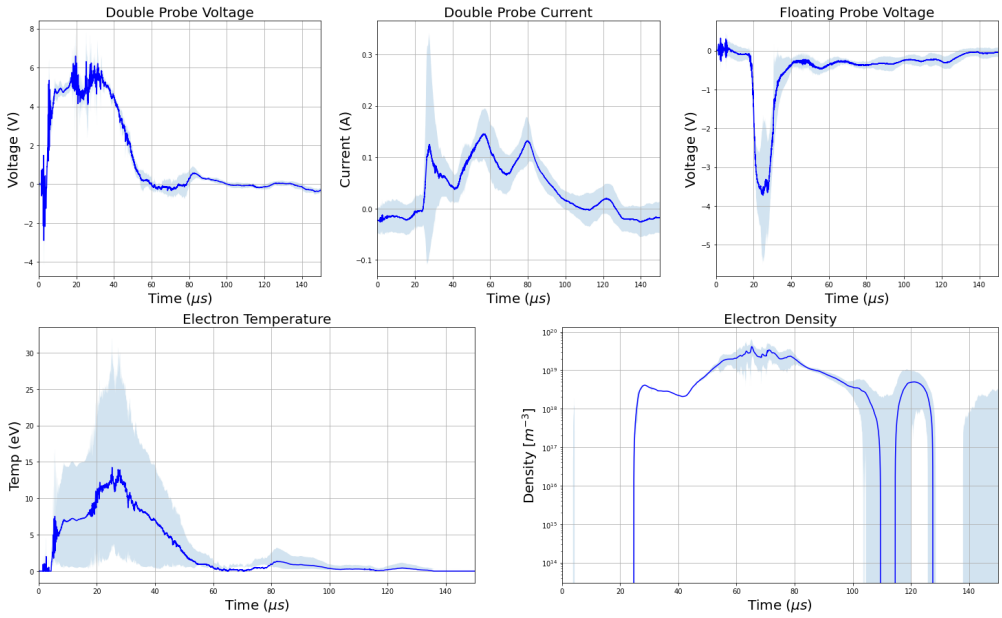

Figure 4.15: Plasma parameter of electron temperature and density along with the triple Langmuir probe signals for $z = 435$ mm and $r = 0$ for the spoked end wall configuration.

4.3 Ion Doppler Spectroscopy Results

The initial spectra seen for the C III line at 229.687 nm was too dim to be seen by the ICCD camera when the original end wall electrode was attached. To combat this, a 50% by pressure mixture of methane was added to the hydrogen gas to increase the number of carbon atoms in the machine. This was successful and IDS spectra was able to be captured, Fig. 4.18a. When the end wall electrode was removed, there was sufficient carbon present in the plasma from the graphite nosecone for bright spectra to been seen, so a pure hydrogen supply gas was used. The impact parameter seen in the graphs refers to what radial position the chord of light was seen from in reference to machine axis. The resulting plasma exhaust speed is directly correlated with the increase in flow through percentage with different end wall configurations.

The furthest right chord had anomalous behavior as can be seen in Fig. 4.19a. This is most likely due to it being at the very bottom of the ICCD camera, being subjected to

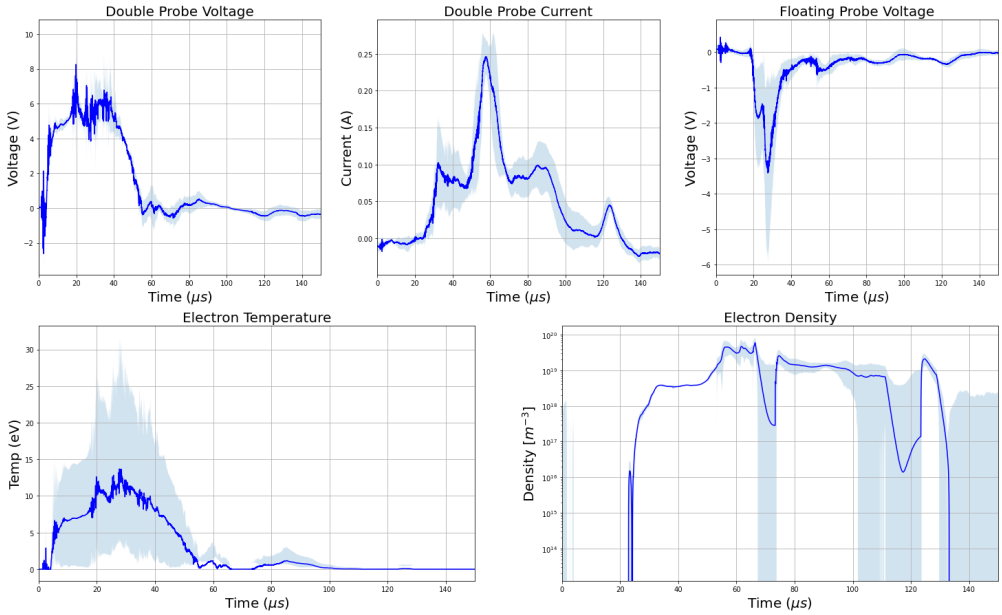

(a) Plasma parameters of electron temperature and density along with the triple Langmuir probe signals for $z = 435$ mm and $r = 20$ mm.

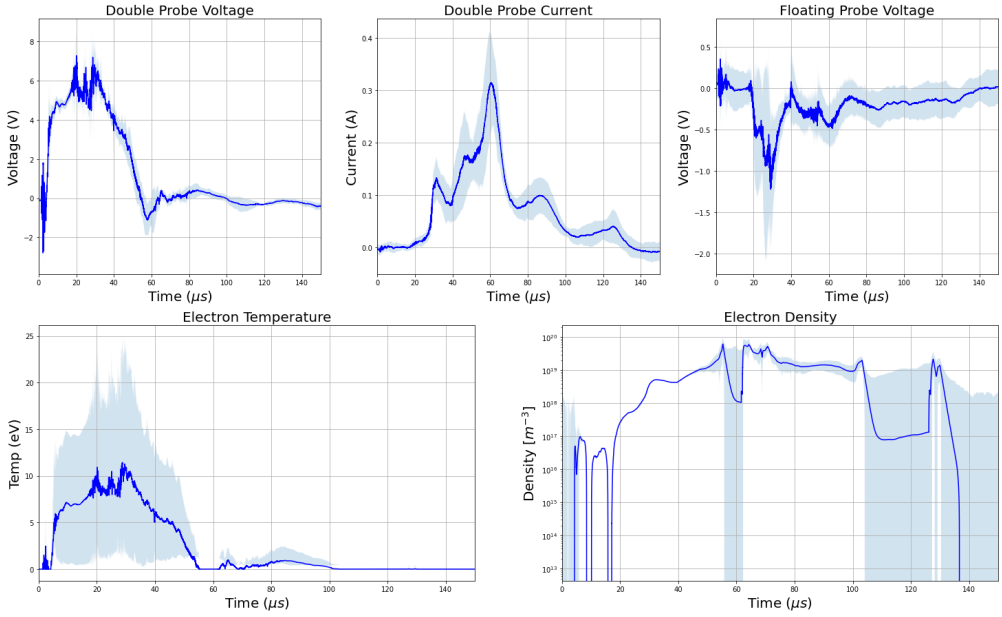

(b) Plasma parameters of electron temperature and density along with the triple Langmuir probe signals for $z = 435$ mm and $r = 40$ mm

Figure 4.16: Comparison of triple Langmuir probe results at $r = 20$ and $r = 40$ at the second axial location with the end wall electrode spoked configuration.

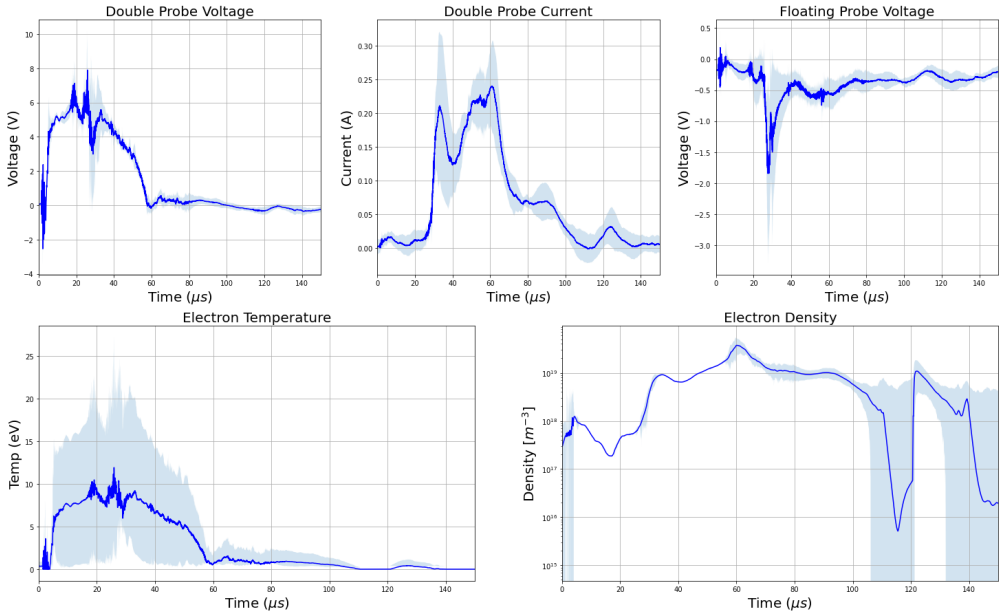

(a) Plasma parameters of electron temperature and density along with the triple Langmuir probe signals for $z = 435$ mm and $r = 60$ mm

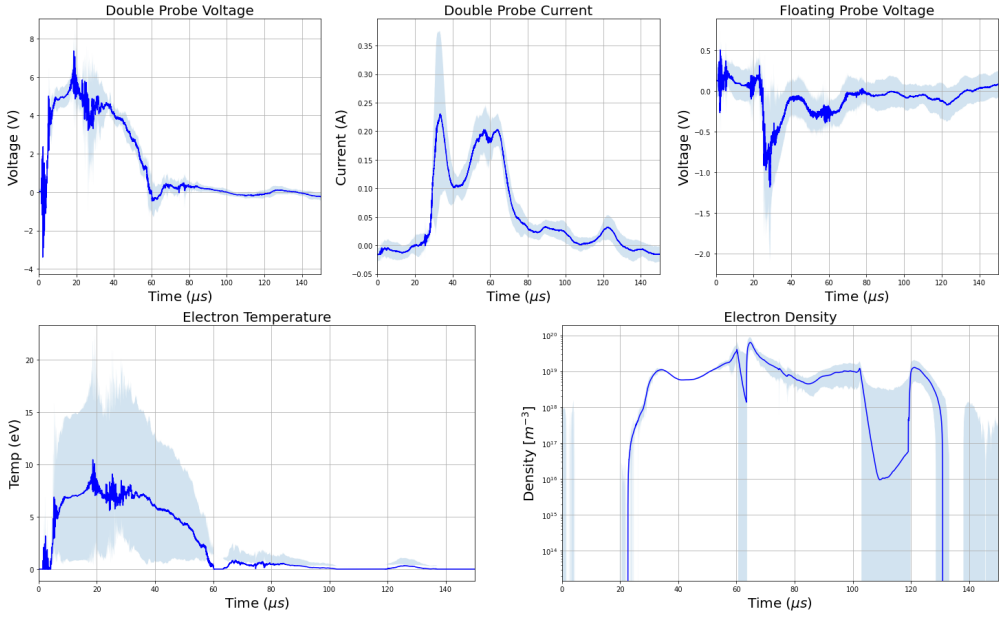

(b) Plasma parameters of electron temperature and density along with the triple Langmuir probe signals for $z = 435$ mm and $r = 80$ mm

Figure 4.17: Comparison of triple Langmuir probe results at $r = 60$ and $r = 80$ at the second axial location with the end wall electrode spoke configuration.

Configuration (Flow Through %)	Average Exhaust Speed
Original (1%)	27 ± 20 km/s
Spoked (55%)	47 ± 19 km/s
Removed (100%)	103 ± 11 km/s

Table 4.1: Plasma exhaust speed increase with flow through percentage. The error in the measurement also decreases as more carbon impurities are in the plume with a large flow through percentage creating brighter spectra.

instrument function errors and possibly not all of its light being collected correctly causing a dimmer signal. This chord is thrown out from data analysis is later sections.

The sheared flow that is present in the assembly region is no longer present. The radial distribution of the flow velocities exhibiting uniformity is evidence of this disappearance of sheared flow. The redistribution of velocities throughout the flow could be a result of the plasma demagnetization forces that occur at the end wall. The uniformity in the exhaust is advantageous for an advanced space thruster as it decreases the possibility of turbulence in the plume. Any energy being put into turbulence would detract kinetic energy of the exhaust, decreasing thrust.

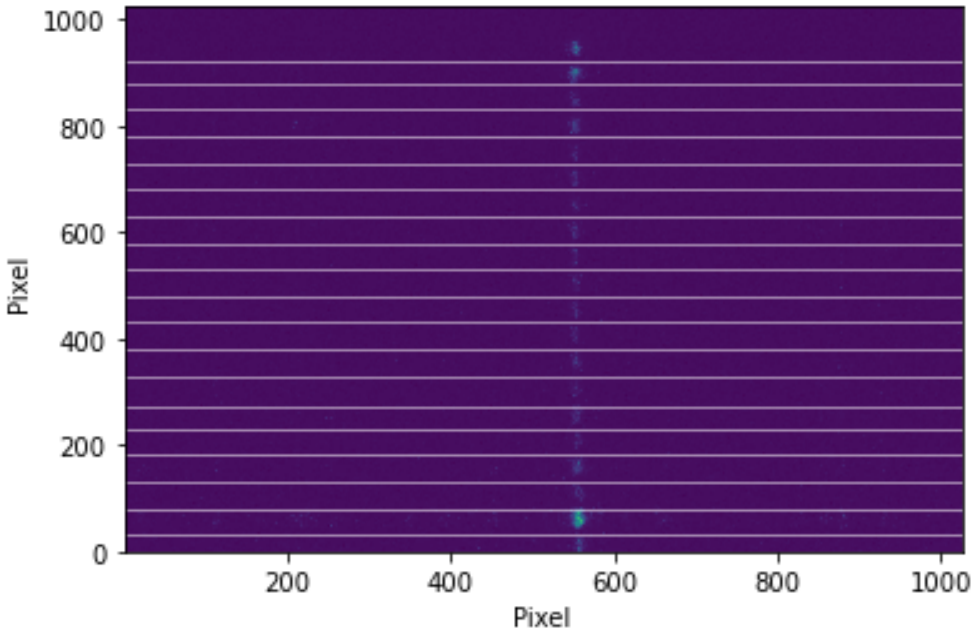

(a) Raw spectra as seen in Light Field from shot 230405013. The spectra being examined is the C III emission at 229.687 nm. The horizontal bin lines are plotted in post to better visually separate the chords.

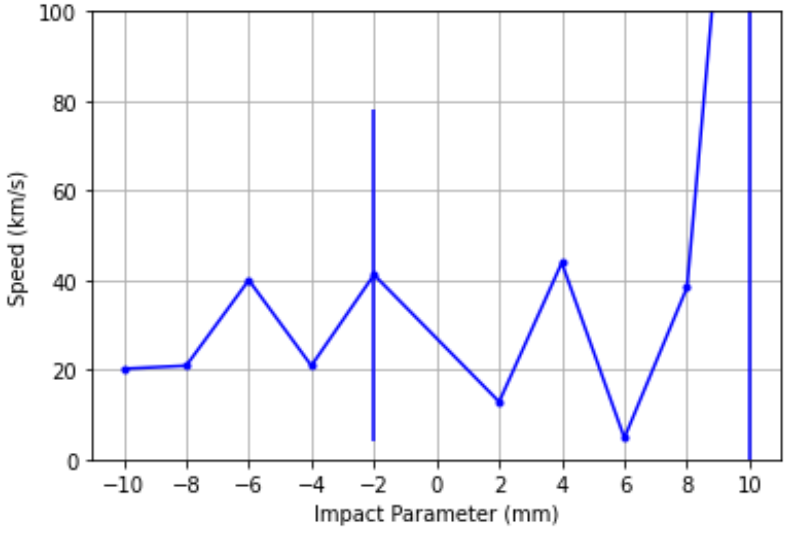

(b) Plasma exhaust speed from ion Doppler spectroscopy with the end wall electrode in place. The impact parameter refers to where the light is coming from relative to the machine axis. An impact parameter of zero is on the machine axis.

Figure 4.18: Example raw C III 229.687 emission spectra and the resulting exhaust speed measurements from the Doppler shift.

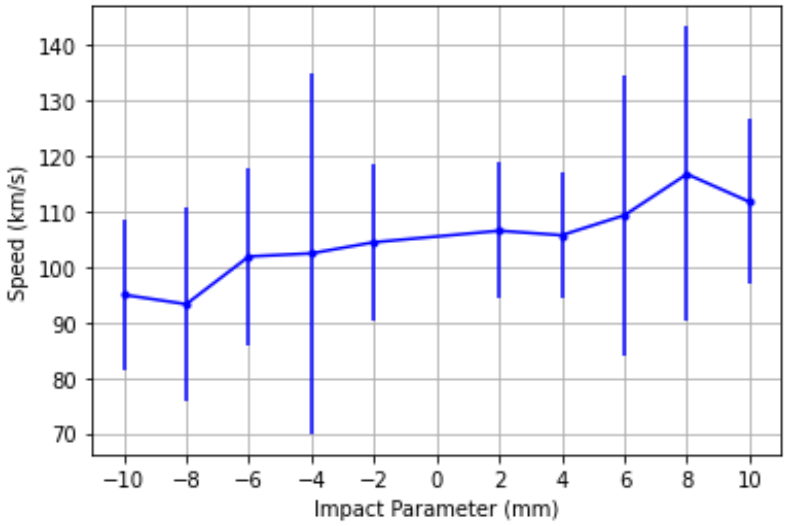

(a) Plasma exhaust speed from ion Doppler spectroscopy with the end wall electrode removed. The impact parameter refers to where the light is coming from relative to the machine axis. An impact parameter of zero is on the machine axis. The chord viewing -8 mm impact parameter was too dim to get reliable data.

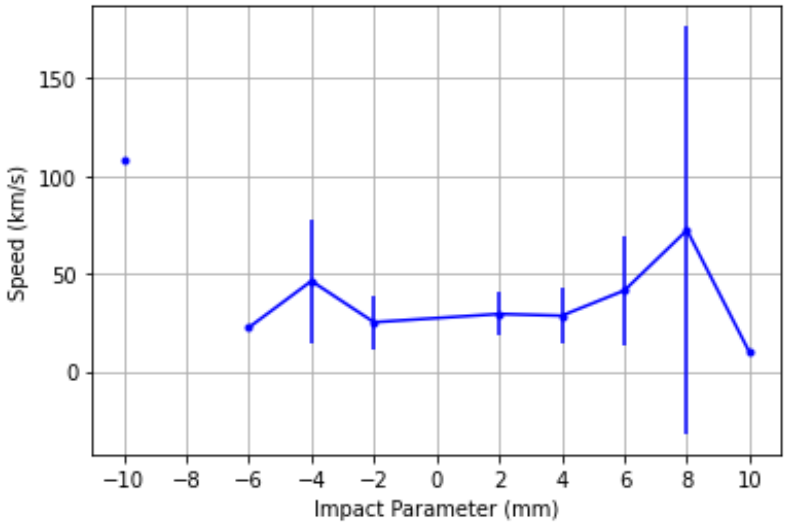

(b) Plasma exhaust speed from ion Doppler spectroscopy with the spoked end wall configuration. The impact parameter refers to where the light is coming from relative to the machine axis. An impact parameter of zero is on the machine axis.

Figure 4.19: IDS results from the end wall being removed and the spoked end wall.

Chapter 5
ANALYSIS AND DISCUSSION

All of the data collected and discussed in the previous chapter must be coalesced in order to make conclusions about the plume and thrust characteristics. The electron density found from the Langmuir probe can be used to find spatial and temporal trends in linear density. This ultimately can be used in conjunction with flow speed data from IDS to determine mass flow rate and thrust. The behavior of the plume itself can be analyzed through the exploration of electron temperature and density gradients in the radial and time domains. This chapter will illustrate the methods used and results of examination of the aforementioned characteristics, setting up conclusions about what type of end wall geometry may be best suited for a space thruster.

5.1 Plume Characteristics

Plume divergence is a key consideration whenever dealing with plasma based propulsion devices. As with any rocket, the majority of the force is from momentum thrust. If there is a significant divergence in the plume, some of that momentum transfer will be radially canceled and not invoke itself on the space craft being propelled. A well collimated beam of plasma is best suited for maximizing the thrust. Additionally, understanding how the plume expands naturally can help inform assumptions for MHD calculations and simulations of the full plume. The makeup of the plume will be investigated first, namely analyzing any radial gradients in temperature or density. Every 20 mm is chosen to be plotted to not over saturate the graph with traces and thus making it unreadable. The trends in this coarse radial resolution are consistent when higher spatial resolution is plotted on multiple graphs as well, Appendix A. A z location of 267 mm shows that, within error, the plume has a

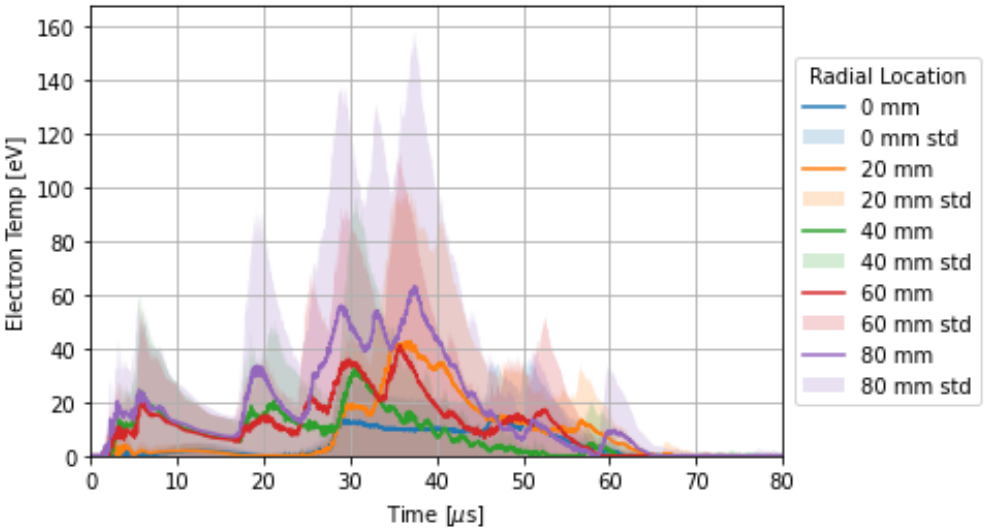

(a) Time evolution of electron temperature at $z = 267$ mm at various radial locations. The trends reveal a uniform temperature plume with the original end wall on.

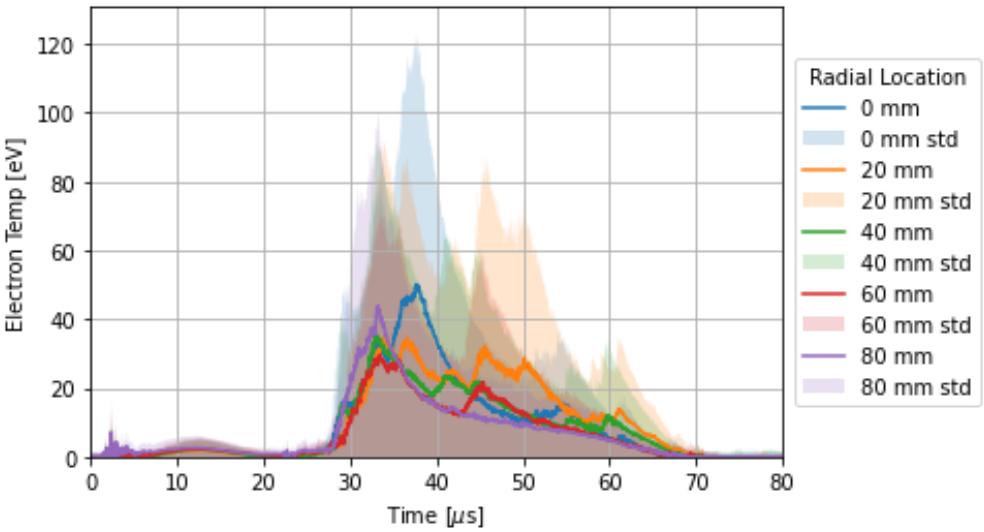

(b) Time evolution of electron temperature at $z = 435$ mm at various radial locations. By this axial location, the plume has further thermally equalized other than a hot core with the original end wall on.

Figure 5.1: Comparison of electron temperature time evolution at both axial locations.

uniform electron temperature distribution during acceleration time: $t < 20$ μs. During initial compression time, 20-30 μs, there exists a temperature gradient toward the outer reaches of the plume. This gradient disappears as the plasma comes to the end of its lifetime. The plume tends to thermalize even further as it progresses downstream and makes it to 435 mm from its exit plane. The increased agreeability between signals farther down the chamber suggest the plume may have large temperature gradients at the exit plane that take time to thermalize. It is intriguing to point out that even as the outer reaches of the plume thermalize, the center of the plume becomes hotter in temperature. The other important implication from the magnitude of the temperatures is that the plume is expanding mostly isothermally. The average temperature of outer locations remains the same. The only outlier that may disagree with that conclusion is the hotter central plume farther downstream that started cooler. This trend of a unique center of the plume continues with the density. The density graphs, Fig. 5.2, being zoomed in on the time axis is two-fold. Firstly, this cropping allows the time interval of interest to be better analyzed. Secondly, as mentioned before, only time intervals that have a physical I-V characteristic trace are analyzed. The time domain shown is the interval in which the I-V trace was valid for all given radial location density measurements. The first z axis location reveals no trends in electron density. Within a standard deviation, the plume may have a mostly uniform electron density. As the plume progresses downstream and has more time to equalize, clear trends start to form. The plume has a direct relation between radius and density. This causes a slight hollowness to the plume. This may turn out to be advantageous for space thruster in this particular instance. From IDS, the sheared flow from the SFS Z Pinch is still present in the plume. A faster moving outer radius of plasma that is more dense will increase the momentum thrust. These gradients all but disappear when the spoked end wall is used.

As was alluded to in the Experiment Results chapter, the electron temperature is uniform when the spoked end wall is installed. The density on the other hand is still quite dynamic by $z = 435$mm unlike with the original end wall on. The magnitude of density is comparable to that of when the end wall is on, suggesting that the mechanism of plasma magnetic

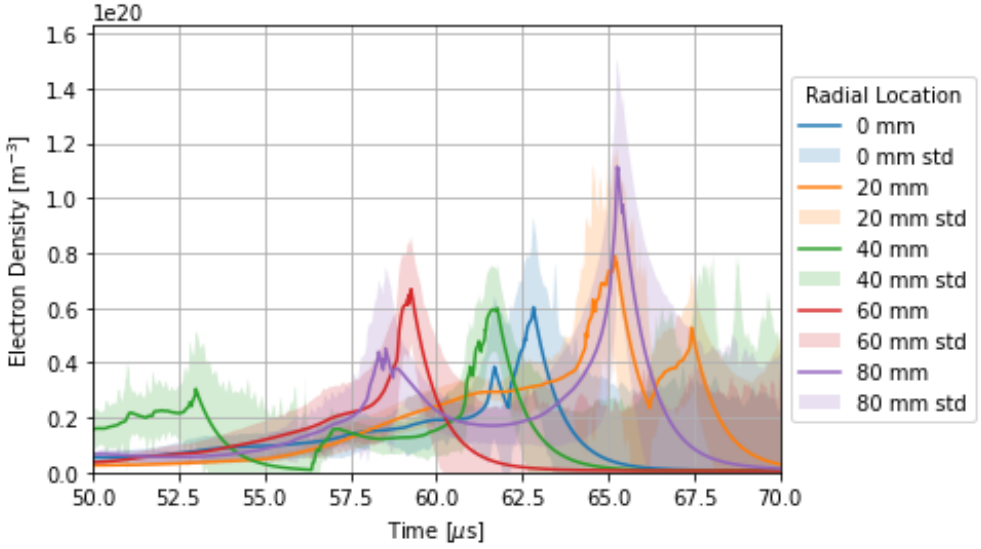

(a) Time evolution of electron density across the radial distribution of the plume at $z = 267$ mm. The time scale has been zoomed in to show relevant physical data based on I-V characteristic reconstructions.

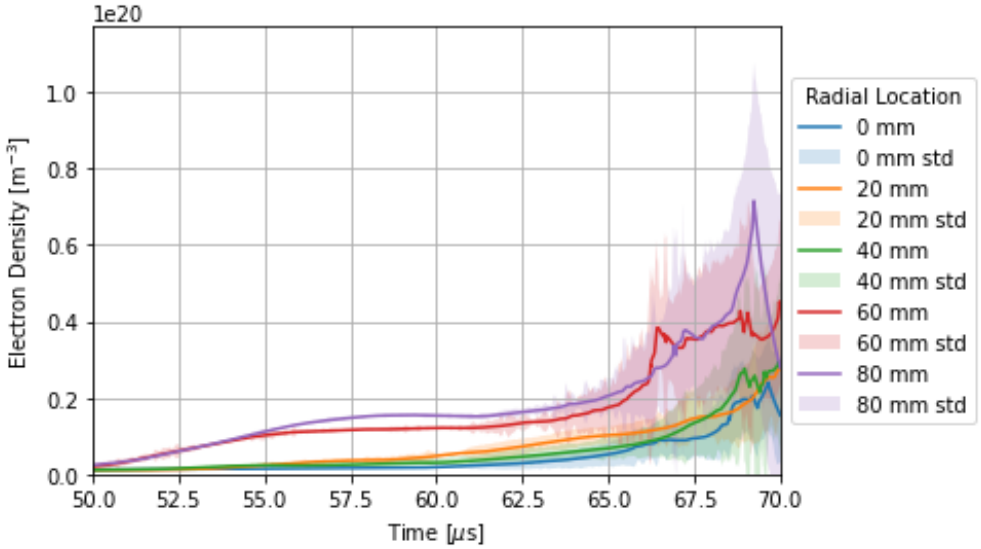

(b) Time evolution of electron density across the radial distribution of the plume at $z = 435$ mm. The time scale has been zoomed in to show relevant physical data based on I-V characteristic reconstructions.

Figure 5.2: Comparison of electron density time evolution at both axial locations.

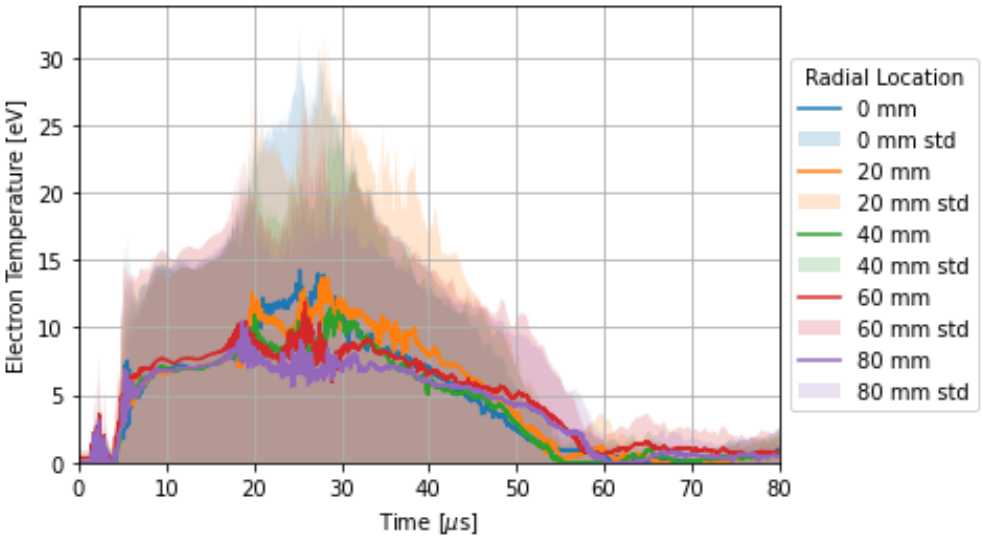

Figure 5.3: Radial variations in electron temperature over the pulse duration for the spoked end wall configuration. This comparison reveals a plume that has uniform electron temperature with a slight outward gradient during peak current time.

detachment is similar between the configurations. Plasma magnetic detachment is discussed in Ref. [5, 15]. As a summary, for the plasma to become demagnetized the plasma ram pressure must exceed the force of the magnetic tension. A higher degree of detachment from the magnetic field should lead to higher densities seen by the Langmuir probe. As the densities are of the same magnitude for original vs spoked, the force balance is independent of end wall configuration. Higher densities are seen with the end wall off since the plasma ram pressure must far exceed the magnetic tension as the outer electrode is no longer acting a flux conserver.

5.2 Thrust Characteristics

Now that a better understanding of the plume's inner characteristics are understood, thrust and impulse can be calculated. The thrust of the end wall electrode being removed created some challenges when performing this calculation. While the original configuration permitted

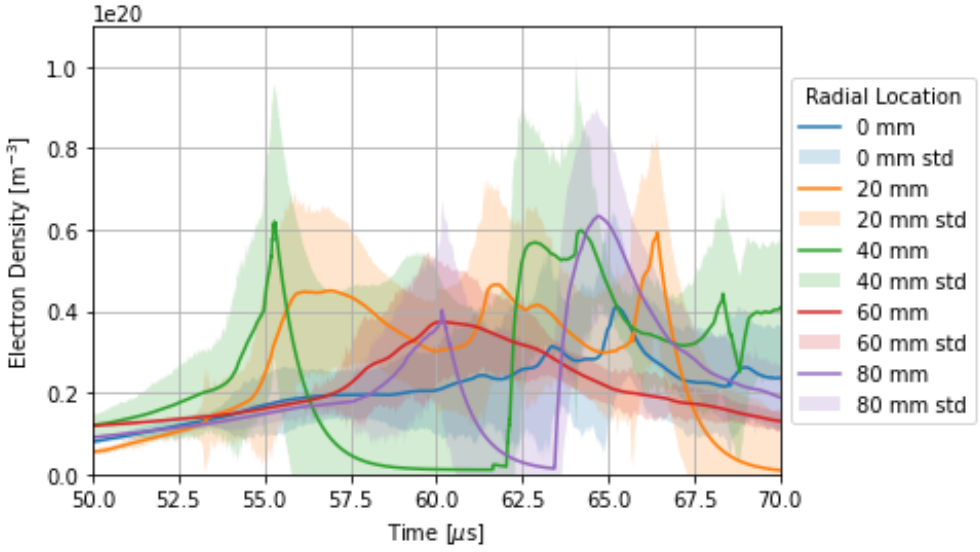

Figure 5.4: Electron density radial variation over the time of the pulse for the spoked end wall configuration. The traces suggest a turbulent plume only small gradients in density.

Langmuir probe measurements at all radial locations, the latter case only had data from r=100 mm as discussed in previous chapters. Having only one spatial location of data required the assumption that the end wall electrode being removed had a constant average density along the radial direction. This assumption is used from the result that there are no clear trends in density in the spoked end wall case, suggesting that as one moves to a higher flow through percentage, the density become more uniform in the radial direction. This assumption may over calculate the thrust produced near the center of the plume, but will under calculate the thrust near the edge if there are any gradients in density. The overall thrust should remain the same.

$$F_T = \dot{m}v + (P_e - P_0)A_e \tag{5.1}$$

The force generated from a rocket nozzle in general can be found from Eq. (5.1). The first term is the momentum thrust with the latter being pressure thrust due to the exit having higher pressure than the surrounding environment.

Mass flow rate can be related to linear density through unit analysis. Mass flow has units of kg/s. Linear density has units of kg/m. If linear density is multiplied by a flow velocity, mass flow rate is found. Linear density (N) is calculated by taking the integral of the radial function of electron density over the area. It is assumed for this calculation that the plume is axisymmetric.

$$N = m \int_0^a n(r) 2\pi r dr \tag{5.2}$$

If the plasma is assumed to act as an ideal gas, the equation of state can be used to find plasma pressure.

$$P_p = n k_b T_e \tag{5.3}$$

The electron density and temperature is known at each time step and spatial location, so pressure gradients can also be found. By substituting known quantities into the thrust equation one obtains an altered thrust equation for ZaP-HD.

$$F_T = N m v^2 + (n k_b T_e - P_0) A_e \tag{5.4}$$

Using this methodology, a thrust versus time graph can be made for both end wall electrode configurations. In each graph the total impulse and specific impulse were also calculated. Total impulse is the area under the thrust vs time graph.

$$I_{tot} = \int F_T dt \tag{5.5}$$

Then specific impulse can be calculated in one of two ways, either Eq. (5.6) or Eq. (5.7).

$$I_{sp} = \frac{I_{tot}}{m g_0} \tag{5.6}$$

$$I_{sp} = \frac{V_e}{g_0} \tag{5.7}$$

The first of these equations was used to calculate the specific impulse from the total impulse and the latter was used to calculate it directly from the flow velocity given by IDS. This shows a very large difference in specific impulse depending on which approach was taken, Table 5.1. This difference can be attributed to the addition of pressure thrust. Eq. 5.7 does

Configuration	I_{sp} from Eq. (5.6)	I_{sp} from Eq. (5.7)	% Difference
End Wall Electrode On	6500 ± 3800 s	3000 ± 2000 s	53%
End Wall Electrode Off	16300 ± 1000 s	10500 ± 1100 s	35%
End Wall Electrode Spoked	7600 ± 4800 s	4600 ± 2000 s	39%

Table 5.1: Specific Impulse calculation method comparison

not take into account the pressure thrust from the exhaust. This illustrates that the pressure thrust is a non-negligible part of the performance of a space thruster using this technology. To more accurately calculate the I_{sp} from Eq. 5.7, the exit velocity needs to be adjusted to the equivalent exit velocity.

$$V_{eq} = V_e + \frac{(P_e - P_0)A_e}{\dot{m}} \tag{5.8}$$

The change is specific impulse seen from this more accurately calculation results in differences that are well below the magnitude of the error. Eq. (5.7) assumes that the equivalent exit velocity and thus the exit pressure and mass flow rate is constant over a pulse. From Fig. 5.5 and Fig. 5.6, it is clear this is not the case. The pulsed nature of this experiment indicates that the total impulse route of calculating specific impulse may be more accurate, as it takes into account the time varying nature of these parameters.

The thrust from the original ZaP-HD configuration produces rather low thrust values as expected. With the majority of the plasma reflecting off the end wall and not being able to make it through the end wall electrode greatly reduces the momentum thrust. In contrast, with the end wall electrode removed, all of the plasma can freely flow out. This also allows for greater speeds as there is no physical barrier in the way of the flow. The trend in increasing thrust with flow through percentage can be fit an an exponential curve, Fig. 5.8. This projected curve suggests that to maximize thrust, no end wall should be present. Further, the steep slope of the exponential near high flow through percentages means that large amounts of potential thrust may be lost from small changes in geometry. Since the stability analysis indicated that the presence of an end wall is beneficial for pinch

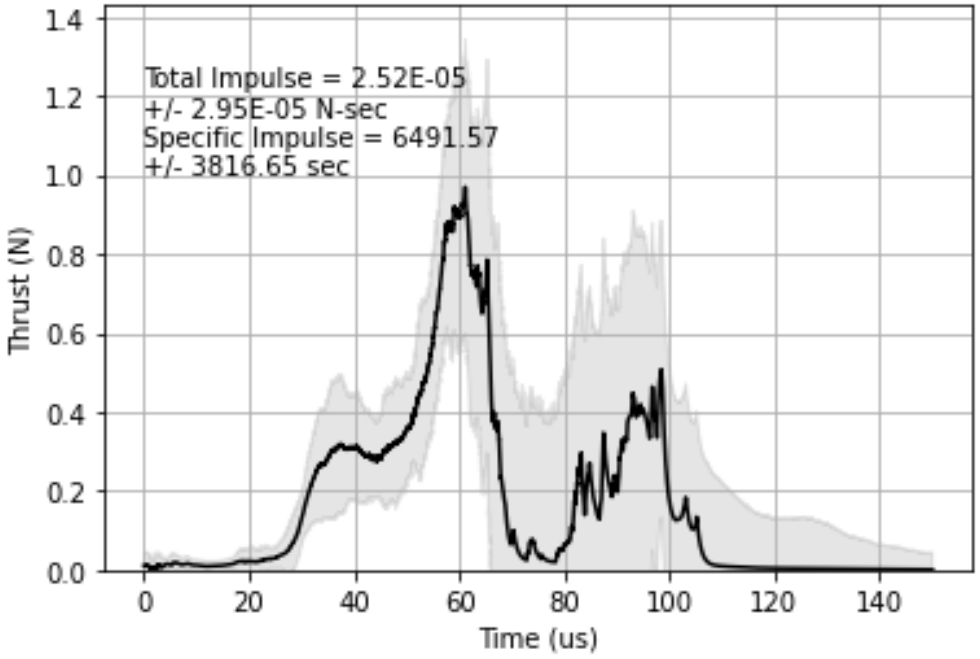

Figure 5.5: Thrust profile for ZaP-HD in the end wall electrode on configuration.

performance, the largest flow through percentage end wall that is structurally sound should be used for an advanced space thruster.

5.3 Plasma Exhaust Demagnetization

In the assembly region of ZaP-HD the plasma is considered to be magnetized. For the plasma to flow freely into the vacuum extension as observed by the Langmuir probe, the plasma must become demagnetized. This event most likely occurs at the plane of the end wall. There is a balance of pressure forces at the end wall that determine if plasma is allowed to flow into the vacuum extension, Fig. 5.9. When the end wall is removed, the outer electrode of ZaP-HD no longer acts as a flux conserver. This change should eliminate any magnetic tension that the plasma ram pressure has to compete with to exit. The kinetic energy of the plume with the end wall removed is $1.14*10^{-17} \pm 8.35*10^{-20}$ joules per particle. This is 85% more energy than with the spoked end wall: $1.69*10^{-18} \pm 3.34*10^{-19}$ joules per particle.

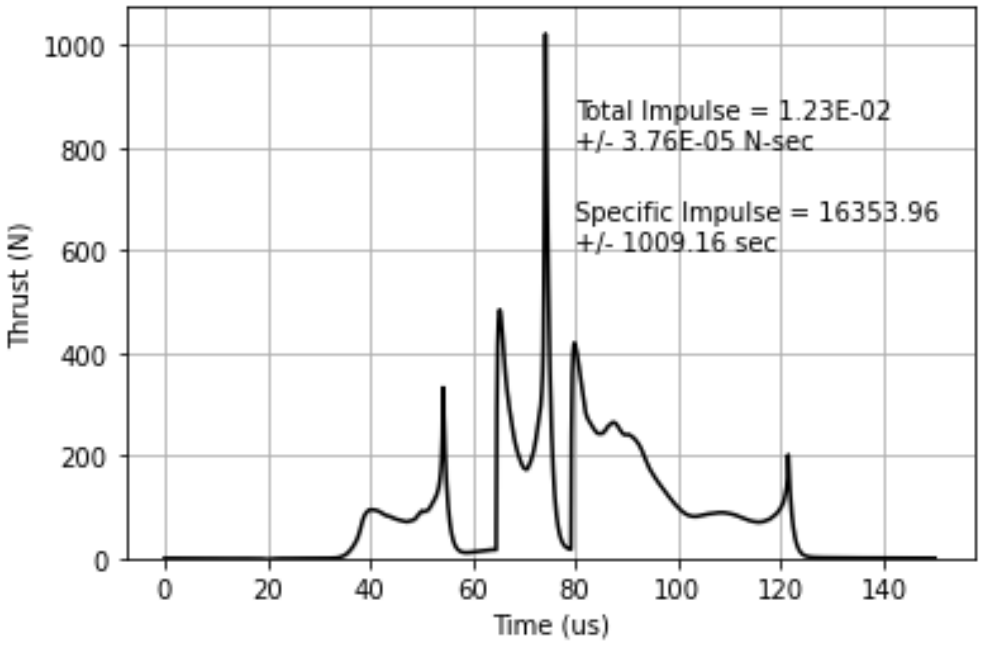

Figure 5.6: Thrust profile for ZaP-HD in the end wall electrode off configuration. This thrust profile does have standard deviation errors, however they are on the order of 10 N so they do not show up on the graph. This thrust curve is not as "smooth" as with the end wall electrode on as a full radial distribution was not able to be measured.

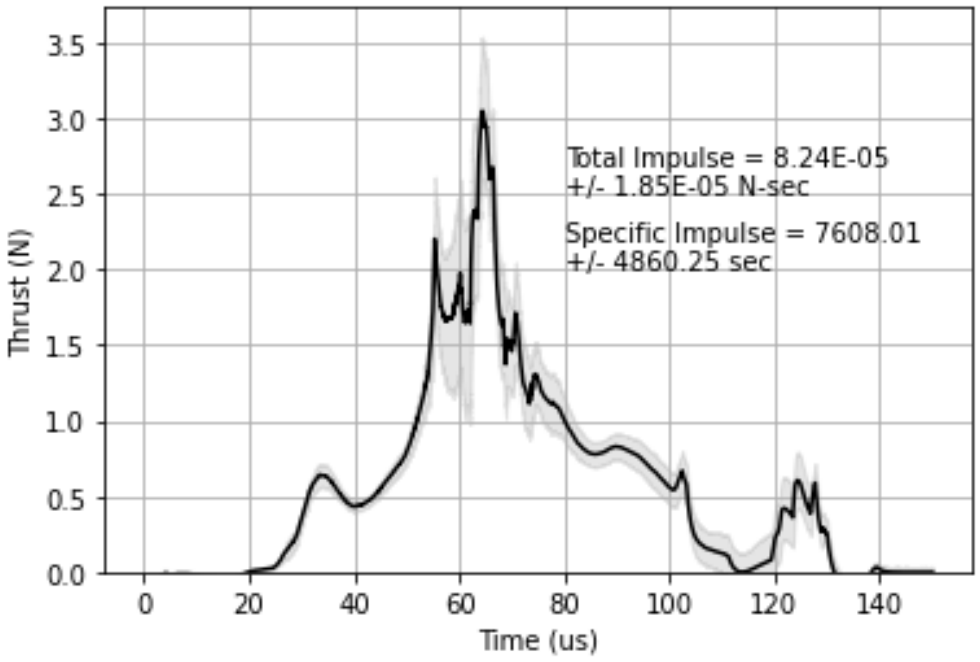

Figure 5.7: Thrust profile for ZaP-HD with the spoked end wall configuration.

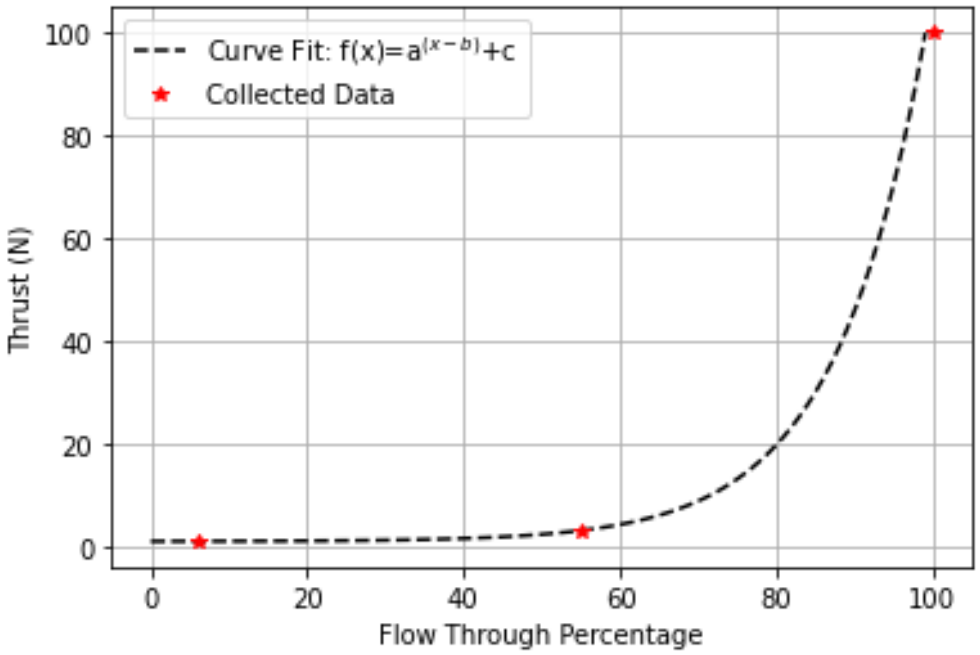

Figure 5.8: Projected exponential trend on the impact of flow through percentage on thrust of ZaP-HD. Fit parameters: a = 1.09, b = 46.8, c = 0.97

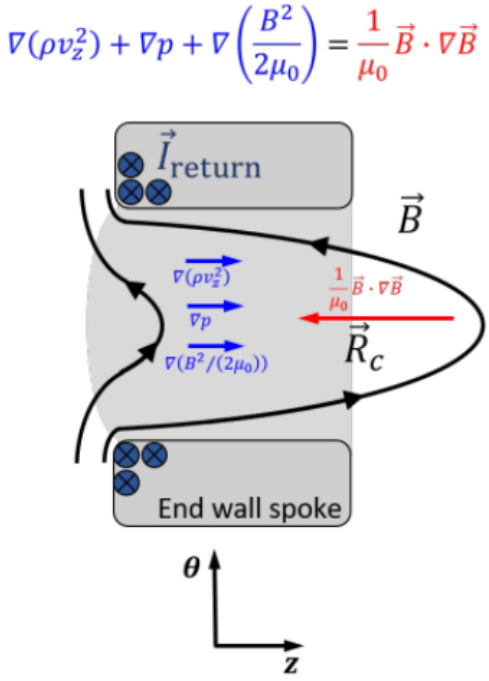

Figure 5.9: Force balance at the spoked end wall of ZaP-HD. The plasma ram pressure must be greater than the magnetic tension in order for the plasma to become demagnetized and exit into the vacuum chamber [5].

This would imply that up to 85% of the kinetic energy of the plasma gets converted into ram pressure to overcome the magnetic forces. A future advanced space thruster would want to mitigate this loss by minimizing the magnetic tension at the exit plane. The reduction is overall mass flow and total mass seen in the vacuum extension can also be explained by this phenomena. The increased magnetic force due to the presence of an end wall inhibits all of the plasma from exhausting from the device. Only the most energetic particles in the plasma can become exhaust. The implications for a future advanced space thruster are fusion condition magnetic fields are much higher than in ZaP-HD. Likewise, the particle energies seen in fusion are also substantially higher. The scaling of the resulting force balance would need to be carefully considered when building a fusion scale SFS Z-Pinch thruster.

Chapter 6

CONCLUSIONS

The methods, experimental results and the accompanying analysis have been completed in the previous sections. Results of thruster performance are compared to existing electric propulsion thrusters and other up and coming future propulsion devices in the research and development phase. Conclusive recommendations for trends in performance vs electrode configurations are drawn. This will inform any future work that can be done to further supplement the knowledge of electrode shaping for shear flow stabilized Z-pinch experiments.

6.1 Experiment Summary

To study the plasma parameters in the exhaust plume of ZaP-HD, a combination of a triple Langmuir probe and ion Doppler spectroscopy was used. The Langmuir probe was mounted on a translation stage allowing for a full radial sweep of plasma parameters. It was assumed that the plume was axisymmetric so a radial sweep and z axis location change was deemed sufficient. This probe would allow the determination of electron temperature and density, both key parameters for characterizing a plasma. A triple probe was chosen as opposed to a single swept probe due to its ability to respond quickly to fast varying plasma potentials. The electron density and temperature profiles provided insight into any gradients and behavior of the plume over time and space. Ion Doppler spectroscopy was useful for determining the speed of the plasma plume. This was necessary as the particle's speed is needed to determine the momentum term of thrust. The C III 229.687 nm emission line was used due to the relative abundance of carbon entrained in the plasma from the carbon nose cone. Addition carbon can also be introduced into the plasma through mixing methane into the supply gas. This C III singlet has a high relative intensity according to the NIST data base.

	End Wall Electrode On	4-Spoke End Wall	End Wall Electrode Removed
e^- Temperature	60 eV	10 eV	20 eV
e^- Density	$6 * 10^{19}$ m^{-3}	10^{21} m^{-3}	$4 * 10^{19}$ m^{-3}

Table 6.1: Tabulated geometry impact on electron parameters.

This results in the highest emission counts on the ICCD camera used to image the emission.

Thirty-four spatial locations were chosen in the vacuum extension in order to give high enough spatial resolution to fully characterize the plume. These consisted of data points from the machine axis (r=0) to 80 mm from machine axis (r=80) at two different axial locations, z = 267 mm and z = 435mm from the end wall exit plane. The axial locations of the measurements were restricted to the spacing of the conflat ports on the vacuum extension vessel. Five shots were taken at each spatial location to provide statistical significance. The IDS data was averaged over a total of ten shots. This increase in statistical significance was enabled by there only being one chord-integrated location for this diagnostic.

6.2 Results Summary

Averaging and smoothing was needed to provide usable voltage and current signals from the Langmuir probe. The SNR for this diagnostic is often low for high energy density plasmas as discussed in previous sections. Despite this, confidence in the data produced was achieved through obtaining uncertainties in the form of standard deviations over numerous shots. Peak plasma parameters found for each configuration are tabulated in Tab. 6.1. If the plasma is considered to behave as an ideal gas in the vacuum extension, some conclusions about the pressure can be drawn. The increase in density is much higher than that of the change in temperature by an order of magnitude. This would indicate an increase in pressure as the plasma slows down and expands from the equation of state. This is the behavior that would be expected from an ideal gas.

The axial variation of the plasma properties reveals other interesting phenomenon. Within

one standard deviation of the plasma temperature, the plasma expands isothermally. The temperature seen at the second axial location is closely comparable to that of the first axial location. The data supporting that the plasma does in fact behave as an ideal gas and expands isothermally are key assumptions that can inform future plasma modeling. This assumption holds for not the entire radial spatial domain, but in two different regimes. The center of the plume tended to be hotter and less dense than the outer shell of the plume. This inner shell extends from the axis to approximately 20 mm from the axis. Within these two respective shells, the assumption of isothermal expansion holds.

The density has a similar uniformity at the first axial location but forms a hollow density gradient as it migrates down in the chamber. This may be due to the shear flow remaining in the vacuum extension as seen in the IDS results. The outer impact parameters have a higher velocity than the inner. From this density profile, a linear density was calculated. When combined with IDS flow velocity data, the thrust of ZaP-HD could be realized. The thrust varied greatly between the two electrode configurations as expected. The more restrictive original configuration did not allow as much plasma to exit through the end wall and instead reflected the plasma. The open end allowed all plasma mass to flow out at significantly higher speeds, 103 km/s vs 27 km/s. This saw a jump in thrust from only 1 N peak to 100 N. The average calculated mass flow that makes it into the vacuum extension was also an order of magnitude higher with the end wall electrode removed: $4 * 10^{-6}$ kg/s vs $8 * 10^{-4}$ kg/s.

The total and specific impulse were calculated from the thrust vs time graphs generated from this analysis. Specific impulse was calculated both directly from flow speed and from the usage of total impulse. These two calculation differed by 42% on average. This large difference was attributed to the direct calculation assuming a steady flow speed and mass flow rate, which is not valid for this experiment. The calculation following the total impulse was taken instead. This yielded a specific impulse of 16300 $\pm$ 1000 sec for the end wall electrode off and 6500 $\pm$ 3800 sec for the end wall electrode being on. These results favor the end wall electrode being removed for a future deep space propulsion device as it increased

all thruster parameters without significantly effecting the pinch performance and stability metrics. It was noted however, during operation arcs were forming between inner and outer electrodes of ZaP-HD more often with the end wall electrode being removed. This is not ideal for the longevity of ZaP-HD. These arcs are seldom observed with the end wall electrode on since the plasma has a place to attached near the center of the end wall electrode and provide a current path. When this end wall electrode is removed, the shortest current path is no longer necessarily through the plasma, and thus arcs occur.

Since ZaP-HD is a pulsed thruster, an effective thrust needs to be calculated to be able to make a direct comparison to steady state electric propulsion systems. The total impulse calculated previously was per pulse, also known as impulse bit. A future space thruster would need to pulse multiple times a second to propel a space craft. Under an operating pulse rate of 10 Hz, ZaP-HD would provide an effective thrust of 123 mN. The higher this pulse rate is pushed, the higher the effective thrust would become. This provides the opportunity for a variably controlled thrust. The ability to alter the thrust from an engine may be desirable in order to perform precise orbital maneuvers. The resulting thrust performance of ZaP-HD falls slightly behind the front running EP technology, while its efficiency is well above any current EP device. A high pulse rate and scaled fusion conditions are necessary for this technology to be considered for an advanced space propulsion device. ZaP-HD does not create any fusion reactions, whereas FuZE does. These extremely energetic particles being released from fusion can dramatically increase the flow velocity. The fusion products must be charged so that they can be guided out the exhaust and not be isentropically released like neutrons. While only two experimental data points exist for Z pinches (ZaP-HD and FuZE), theory agrees that thrust scales with fusion conditions. A future advanced space propulsion system would need an end wall electrode with high flow through, high pulse rate, and high gain fusion conditions to be a viable thruster.

Device Name	Thrust (N)	I_{sp} (s)
High TRL Devices		
Aerojet BPT-4000 Hall-effect Thruster	0.254	2020
Aerojet AEPS	.6	2800
Low TRL Devices		
VX-200	6	5000
ZaP-HD	0.123	16000
FuZE	2.47	8920
Shumlak's Theoretical $D-He^3$ Engine	$3.3*10^5$	$3.5*10^5$

Table 6.2: Rocket engine performance comparison between current electric propulsion devices and other up and coming technologies. Data from Ref. [1, 8].

Chapter 7
FUTURE WORK

The first and foremost piece of future work that could be done is to add to the already existing data pool and increase the level of confidence in the resulting data. Beyond this, higher radial resolution may also provide more insights to the exact behavior of electron temperature and density gradients this analysis may have missed. Likewise, better axial resolution would also be helpful, although increasing the axial resolution would require a new set up as the current vacuum extension does not support this. Experimenting with more flow through percentages would also better provide insight into any performance curve that may illuminate itself from having more data than just at the two extreme ends. ZaP-HD also can be equipment with a direct force measurement razor pendulum. Running pulses with this to attempt to corroborate with the indirect thrust measurements validity. This may be the most interesting piece of future work as it would be a great validation step of the major methods and assumptions used in this thesis. Obtaining experimental data for higher fusion gain thrust parameters would also be an interesting study to see if experimentation lines up with the theoretical scaling.

BIBLIOGRAPHY

[1] Aerojet rocketdyne solar electric propulsion.

[2] Europa clipper mission.

[3] Matteo Barbarino. What is nuclear fusion? *IAEA Department of Nuclear Sciences and Applications*.

[4] Francis F. Chen. Langmuir probe diagnostics, 2003.

[5] Elliot L Claveau. Axial evolution of a sheared-flow-stabilized z pinch, 2020.

[6] Phil Davis and Steve Carney. Missions cassini, 2023.

[7] E.G. Forbes et. al. Diagnostic development for spatio-temporal resoution of a sheared-flow-stabilized z pinch. *61st Annual Meeting of APS-DPP. Fort Lauderdale*.

[8] Uri Shumlak et. al. Advanced space propulsion based on the flow-stabilized z-pinch fusion concept. 2006.

[9] Uri Shumlak et. al. Roadmap to a compact fusion device based on the sheared flow stabilized z-pinch. ARPA-E Fusion Workshop, 2019.

[10] Michelle Graebner. Measuring electron temperature and density of a sheared-flow z-pinch plasma exhaust plume. 2021.

[11] Walt Kester. What the nyquist criterion means to your sampled data system design. *Analog Devices Inc.*, 2008.

[12] Eric J. Pencil Nicole J. Meckel Lynn A. Arrington, Tom W.Haag. A performance comparison of pulsed plasma thruster electrode configurations. *IEPC*.

[13] M. Y. Naz and A. Ghaffar et. al. Double and triple langmuir probes measurements in inductively coupled nitrogen plasma. *Progress in Electromagnetics Research*, 114, 2011.

[14] et. al. Nikolaos A. Gatsonis. Current-mode triple and quadruple langmuir probe methods with applications to flowing pulsed plasmas. *IEEE Transactions on Plasma Science*, 32, 2004.

[15] Collin Parsons. Characterizing the plasma exhaust plume from a sheared-flow stabilized z-pinch, 2020.

[16] A S Pashchina and R E Karmatsky. Using triple langmuir probe method for study high-speed plasma flow created by a pulsed capillary discharge. *Journal of Physics*, XVII, 2018.

[17] Nikolaos A Catsonis Robert Eckman, Lawrence Byrne. Triple langmuir probe measurements in the plume of a pulsed plasma thruster. *Journal of Propulsion and Power*, 17, 2001.

[18] Dr. David R. Williams. Nasa space and science data coordinated archive.

Appendix A

ADDITIONAL RESULT PLOTS

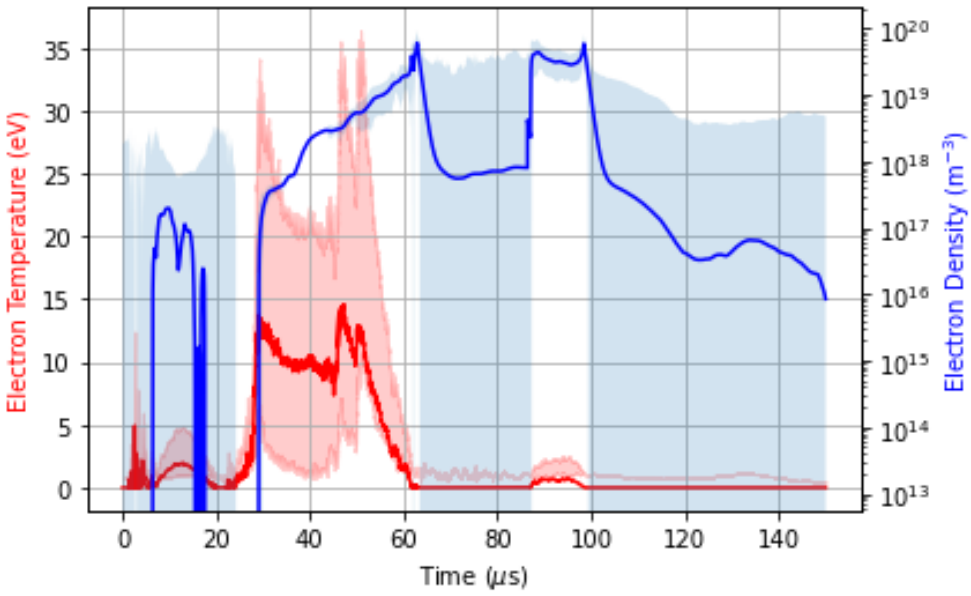

Figure A.1: Langmuir probe data from the original end wall on, r = 0, z = 267. The electron temperature and density are overlayed on the same plot to enable better correlation of how rise times compare.

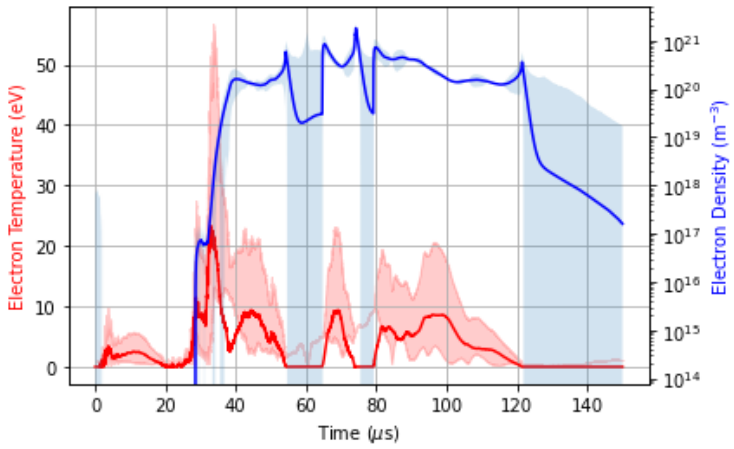

Figure A.2: Langmuir probe data from the end wall removed, r = 100, z = 603. The electron temperature and density are overlayed on the same plot to enable better correlation of how rise times compare.

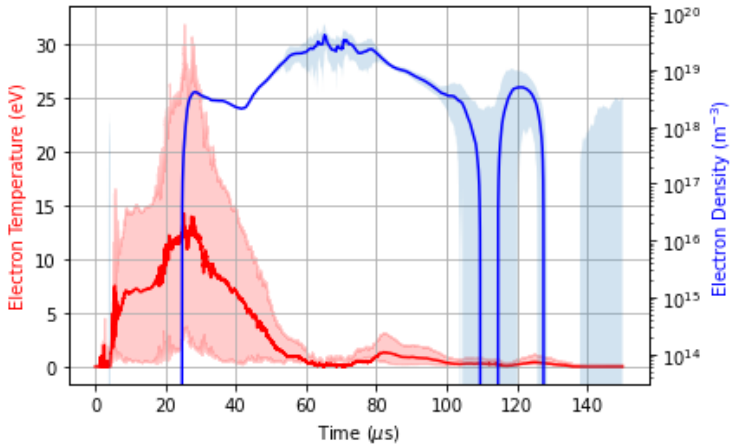

Figure A.3: Langmuir probe data from the spoked end wall on, r = 0, z = 435. The electron temperature and density are overlayed on the same plot to enable better correlation of how rise times compare.

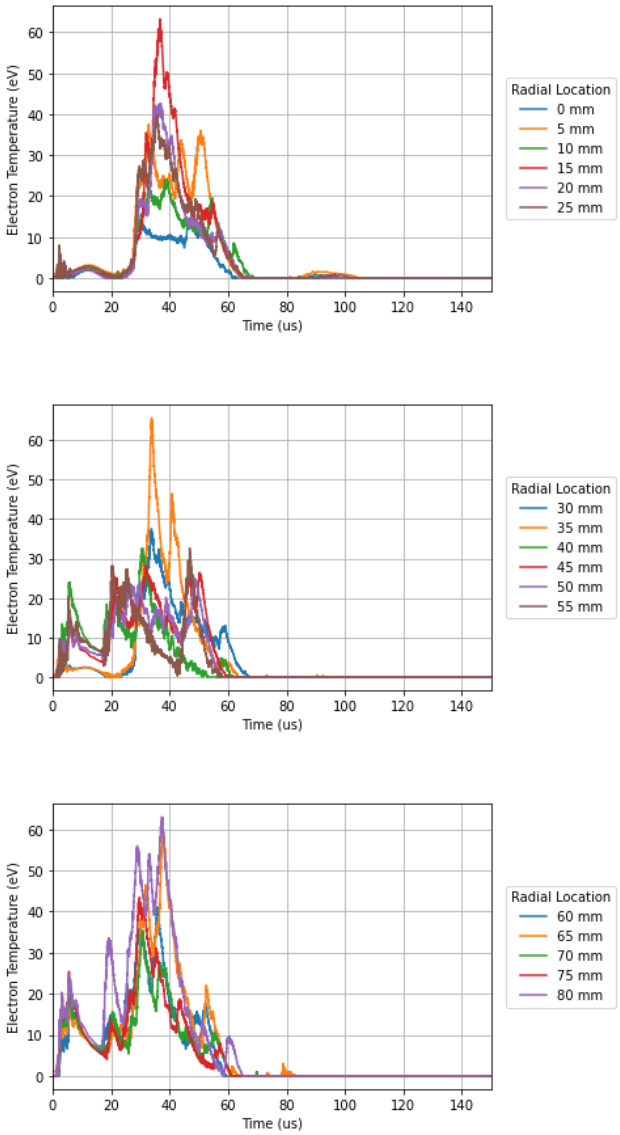

Figure A.4: Higher resolution look at the electron temperature gradients for the original end wall being attached.

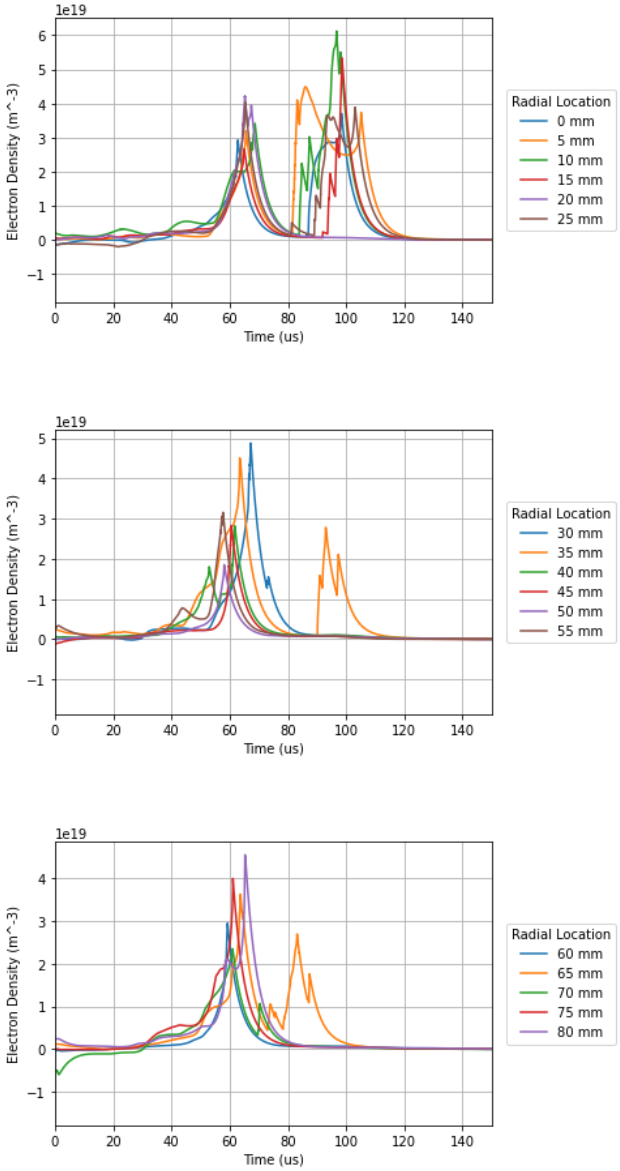

Figure A.5: Higher resolution look at the electron density gradients for the original end wall being attached.

Appendix B

PYTHON CODE

B.1 File Renamer

```python
# -*- coding: utf-8 -*-
"""
Created on Thu Jan 26 20:01:08 2023

Takes the tek files output from the outscope and changes them to
the corresponding shot numbers.

@author: Jared
"""

import os
import glob


def renamer():
    path = 'D:/Zap_data_analysis/Voltage_mode/5_22_23/'
    new_path = 'D:/Zap_data_analysis/Voltage_mode/spoked_end_wall/second_flange/'
    shot = 13
    for filename in glob.glob(path + '*.csv'):
        old_name = filename
        new_name = new_path + str(230522000+shot) + '.csv'
        os.rename(old_name, new_name)
        shot += 1



if __name__ == '__main__':
    renamer()

```

B.2 Langmuir Probe Analysis Code

```
# -*- coding: utf-8 -*-
"""
Created on Sat Jul 30 14:46:18 2022

This script has many functions when it comes to analyzing the raw Langmuir probe data. See each section
description for what they do. In order for this script to analyze the data, a few things need to be set up first.

1) A shot sheet needs to be made. This is a .csv file with column headers of 'Radial Position', 'First Flange', 'Second Flange', 'Third Flange'.
Each cell then has the coresponding shot numbers for that given location. Each shot can be separated by commas or for sequential shots
can be formatted like 230407007-2304010

2) All shots need to be place in a folder of your choosing, but named according to their shot and not the tek000 that is output by the oscope.
There is a file renamer to do this.

This code also assumes you are using a 4 ms window with the scope being triggered 2 ms before the pulse.

@author: Jared
"""

import pandas as pd
import matplotlib.pyplot as plt
import numpy as np
from operator import add,sub
import os
import matplotlib.animation as animation
from scipy.integrate import simpson
from decimal import Decimal


plt.rcParams['axes.grid'] = True


def smooth(data, alpha, offset = False):
    '''
    Smooths data by exponential weight function value alpha. Larger number smooths more.
    If you would like the data to be offset by the background value of the signal, set offset to be True
    when you call the function
    '''
    if offset == True:
        offset = sum(data[0:100])/len(data[0:100])
        data = data - offset
    numbers_series = pd.Series(data)
    moving_averages = numbers_series.ewm(alpha = alpha, adjust = False).mean()
    data_avg = moving_averages.tolist()
    return data_avg


def avg(directory, data_list, pulse_offset, flange, skip=20):
    '''
    This function takes the file path to the directory
    where all of the tek files are stored along with a list
    of file names of data that were taken at a given
    langmuir probe position. Returns a data file of the
    averages of the data is data_list. By default the csv
    files need to have 20 rows skipped. If this changes, the rows
    to be skipped can also change with input skip. Also returns
    the time array in micro seconds.
    '''
    float_volt = []
    double_volt = []
```

```
    double_curr = []

    for data in data_list:
        raw_data = pd.read_csv(directory + flange + '/' + data, skiprows = skip,
        dtype=object).astype(float)
        raw_float = raw_data['CH1']*101
        raw_double_volt = raw_data['CH2']*101
        raw_double_curr = raw_data['CH3']*10
        float_volt.append(smooth(raw_float, 0.001, True))
        double_volt.append(smooth(raw_double_volt, 0.001,True))
        double_curr.append(smooth(raw_double_curr, 0.001,True))

    time = raw_data['TIME']*10**6-pulse_offset
    time_start = time[time == 0].index[0]
    time_end = time[time==150].index[0]
    float_avg = np.average(float_volt,axis=0)[time_start:time_end]
    double_volt_avg = np.average(double_volt,axis=0)[time_start:time_end]
    double_curr_avg = np.average(double_curr,axis=0)[time_start:time_end]

    float_std = np.std(float_volt,axis=0)[time_start:time_end]
    double_volt_std = np.std(double_volt,axis=0)[time_start:time_end]
    double_curr_std = np.std(double_curr,axis=0)[time_start:time_end]

    return (float_avg, float_std), (double_volt_avg, double_volt_std),
    (double_curr_avg, double_curr_std), time[time_start:time_end]


def get_electron_temp_linear(double_current, phi_float):
    '''
    Calculates electron temperature based on a linear assumption that the
    double probe bias voltage is significantly larger than the plasma
    temperature. Takes a list of the double probe voltages and floating
    voltages and returns the electron temperature for each time step.
    '''
    e = 1.602*10**-19
    k = 1.38*10**-23
    keV = 8.617*10**-5
    Vd2 = [double - phi_float for double, phi_float in (double_current, phi_float)]
    return [((e*volt)/(np.log(2)*k))*keV for volt in Vd2]


def get_electron_temp(Vd3, Vd2_list, Vd2_errors):
    '''
    Takes the bias voltage, Vd3 and the difference between the double probe voltage
    and the floating voltage and its corresponding errors. Numerically solves the
    the function for electron temperature and outputs the calculated temp and the
    propagation of error for both high and low as they will be different for
    electron temp
    '''
    e = 1.602*10**-19
    k = 1.38*10**-23
    keV = 8.617*10**-5
    Te_list = []
    Te_errors_up = []
    Te_errors_down = []
    for Vd2, Vd2_error in zip(Vd2_list, Vd2_errors):
        if Vd2 < 0.001:
            Vd2 = 0.001
        Te_guess = 70
        margin = 1
        while margin > 0.1:
            Te = e * Vd2 / (k*(np.log(2) - np.log(1+np.exp(-e*Vd3 / (k*Te_guess)))))
            margin = abs(Te-Te_guess)*keV
            Te_guess = Te
            Te_error_up = e * (Vd2+Vd2_error) / (k*(np.log(2) - np.log(1+np.exp(-e*Vd3
            / (k*Te_guess)))))
            Te_error_down = e * (Vd2-Vd2_error) / (k*(np.log(2) -
```

```
                np.log(1+np.exp(-e*Vd3 / (k*Te_guess)))))
            Te_errors_up.append(Te_error_up*keV)
            Te_errors_down.append(Te_error_down*keV)
            Te_list.append(Te*keV)

    return (Te_list, Te_errors_up, Te_errors_down)


def get_electron_density(double, phi_float, double_current, electron_temp, Vd2_list, Vd2_errors):
    '''
    Calculates the electron density from known Langmuir Probe signals and the electron temp. Outputs
    the electron density and its corresponding error.
    '''
    mi = 1.6726*10**-27
    r_probe = 0.025*2.54*0.01 # Probe radius (m)
    l_probe = 0.066*2.54*0.01 # Probe length (m)
    S = (np.pi*r_probe**2 + l_probe*np.pi*2*r_probe)
    e = 1.602*10**-19
    kb = 1.38*10**-23 #J/K
    keV = 8.617*10**-5 #eV/K
    k = kb/keV #J/eV
    ne = []
    ne_errors = []
    #ne_errors_low = []
    for I3, Te, Vd, dI3, dTe_up,dTe_low, dVd in zip(double_current[0], electron_temp[0], Vd2_list, double_current[1], electron_temp[1],electron_temp[2], Vd2_errors):
        if Te == 0:
            Te = 0.01
        if Vd < 0.01:
            Vd = 0.01

        n = ((I3)/(np.exp(-0.5)*S*e*np.sqrt(k*Te/mi)))*((np.exp(-e*Vd/(k*Te)))/(1-np.exp(-e*Vd/(k*Te))))
        if Te-dTe_low > 0.1:
            ne_error = ((I3+dI3)/(np.exp(-0.5)*S*e*np.sqrt(k*(Te-dTe_low)/mi)))*((np.exp(-e*(Vd+dVd)/(k*(Te-dTe_low))))/(1-np.exp(-e*(Vd+dVd)/(k*(Te-dTe_low)))))
        else:
            ne_error = 0
        ne.append(n)
        ne_errors.append(ne_error)
    ne = smooth(ne,0.005)
    #ne_errors = smooth(ne_errors,0.001)
    return ne, ne_errors

def make_shot_list(position, config):
    '''
    Makes a list of shots to be analyzed. Give a radial position and end wall
    configuration to load the right shot sheet
    '''
    if config == 'On':
        shot_sheet = pd.read_csv('D:/Zap_data_analysis/Voltage_mode/Langmuir_shot_sheet.csv').set_index('Radial Position')
    elif config == 'Off':
        shot_sheet = pd.read_csv('D:/Zap_data_analysis/Voltage_mode/Langmuir_shot_sheet_no_endwall.csv').set_index('Radial Position')
    elif config == 'Spoked':
        shot_sheet = pd.read_csv('D:/Zap_data_analysis/Voltage_mode/Langmuir_shot_sheet_spoked.csv').set_index('Radial Position')
    else:
```

```
176             print('Use either On, Off, or Spoked')
177             return np.nan
178         interest = shot_sheet.loc[position[0],position[1]]
179         data_list = []
180         shot_spans = interest.split(',')
181         for shot_span in shot_spans:
182             for shot in range(int(shot_span.split('-')[0]), int(shot_span.split('-')[-1])+1):
183                 data_list.append(str(shot)+'.csv')
184         return data_list
185 
186 
187 #%%
188 '''
189 This section will process the raw data and graph a single position. It generates 5
    subplots on one graph or 4 plots with the electron
190 density and temperature overlayed.
191 '''
192 
193 '''
194 Inputs
195 '''
196 position = [0, 'First Flange']
197 data_list = make_shot_list(position, 'On')
198 pulse_offset = 2000
199 file_path = 'D:/Zap_data_analysis/Thesis_data/Lab_data/End Wall On/'
200 
201 ################################################################################
    ########################
202 
203 # Get the data
204 floating, double_voltage, double_current, time = avg(file_path, data_list,
    pulse_offset, position[1])
205 
206 #Calculate electron temperature linearly
207 #electron_temp = get_electron_temp_linear(double_voltage_smooth, floating_smooth)
208 Vd2_list = [double - phi_float for double, phi_float in zip(double_voltage[0],
    floating[0])]
209 Vd2_errors = [np.sqrt(double**2 + phi_float**2) for double, phi_float in
    zip(double_voltage[1], floating[1])]
210 
211 #Calculate electron temperature numerically
212 electron_temp = get_electron_temp(200, Vd2_list, Vd2_errors)
213 
214 #Calculate electron density
215 electron_density = get_electron_density(double_voltage, floating, double_current,
    electron_temp, Vd2_list, Vd2_errors)
216 
217 
218 #Plot 5 separate graphs
219 
220 plt.figure(figsize = (25,15))
221 plt.subplot(2,3,1)
222 plt.plot(time, double_voltage[0], 'b-')
223 plt.fill_between(time, double_voltage[0] - double_voltage[1], double_voltage[0] +
    double_voltage[1], alpha=0.2)
224 plt.xlabel(r'Time ($\mu s$)', fontsize=20)
225 plt.ylabel('Voltage (V)', fontsize=20)
226 plt.title('Double Probe Voltage', fontsize=20)
227 plt.xlim([0,150])
228 
229 plt.subplot(2,3,2)
230 plt.plot(time, double_current[0], 'b-')
231 plt.fill_between(time, double_current[0] - double_current[1],
    double_current[0]+double_current[1], alpha = 0.2)
232 plt.xlabel(r'Time ($\mu s$)', fontsize=20)
233 plt.ylabel('Current (A)', fontsize=20)
234 plt.title('Double Probe Current', fontsize=20)
```

```
plt.xlim([0,150])

plt.subplot(2,3,3)
plt.plot(time, floating[0], 'b-')
plt.fill_between(time, floating[0]-floating[1], floating[0]+floating[1], alpha = 0.2)
plt.xlabel(r'Time ($\mu s$)', fontsize=20)
plt.ylabel('Voltage (V)', fontsize=20)
plt.title('Floating Probe Voltage', fontsize=20)
plt.xlim([0,150])

plt.subplot(2,2,3)
plt.plot(time, electron_temp[0], 'b-')
plt.fill_between(time, list(map(sub,electron_temp[0], electron_temp[2])), list(map(add,
electron_temp[0], electron_temp[1])), alpha = 0.2)
plt.xlabel(r'Time ($\mu s$)', fontsize=20)
plt.ylabel('Temp (eV)', fontsize=20)
plt.title('Electron Temperature', fontsize=20)
plt.xlim([0,150])


plt.subplot(2,2,4)
plt.plot(time, electron_density[0], 'b-')
plt.fill_between(time, list(map(sub,electron_density[0], electron_density[1])),
list(map(add, electron_density[0], electron_density[1])), alpha = 0.2)
plt.xlim([0,150])
#plt.ylim([0,None])
plt.title('Electron Density', fontsize=20)
plt.xlabel(r'Time ($\mu s$)', fontsize=20)
plt.ylabel(r'Density [$m^{-3}$]', fontsize=20)
plt.yscale('log')

plt.show()

# #Plot electron temp over electron density
# fig, ax1 = plt.subplots()
# ax2 = ax1.twinx()
# ax1.plot(time, electron_temp[0], 'r-')
# ax1.fill_between(time, list(map(sub,electron_temp[0], electron_temp[2])),
list(map(add, electron_temp[0], electron_temp[1])), alpha = 0.2, color = 'red')
# ax2.plot(time, electron_density[0], 'b-')
# ax2.fill_between(time, list(map(sub,electron_density[0], electron_density[1])),
list(map(add, electron_density[0], electron_density[1])), alpha = 0.2)
# ax2.set_yscale('log')
# ax1.set_xlabel(r'Time ($\mu$s)')
# ax1.set_ylabel('Electron Temperature (eV)', color = 'blue')
# ax2.set_ylabel(r'Electron Density (m$^{-3})$', color = 'red')
# plt.grid()
# plt.show()


#%%
'''
This section Creates a pandas data frame with the calculated avg electron temperature
and avg density for all data in a specified directory
'''

'''
Inputs
'''
pulse_offset = 2000
file_path = 'D:/Zap_data_analysis/Thesis_data/Lab_data/End Wall On/'
config = 'On'
r_start = 0
r_end = 80
rstep = 5
#Shot ranges for each position

```

```
297 ##############################################################################################
298 data_dic = {}
299 i = 1
300 parameter_df_1 = pd.DataFrame()
301 parameter_df_2 = pd.DataFrame()
302 for root, dirs, files in os.walk(file_path):
303     for flange in dirs:
304         flange_dic = {}
305         for rad_pos in range(r_start,r_end+1, rstep):
306             shots = make_shot_list([rad_pos, flange], config)
307             flange_dic[rad_pos] = shots
308         data_dic[flange] = flange_dic
309 
310 for flange, radius_dict in data_dic.items():
311     pd_data = []
312     print('Analyzing Flange: ' + flange)
313     for radius, shots in radius_dict.items():
314         data_list = []
315         print('Analyzing Radius: ' + str(radius))
316         for shot in shots:
317             if os.path.isfile(file_path + flange + '/' +shot):
318                 data_list.append(shot)
319 
320         # Get the data
321         floating, double_voltage, double_current, time = avg(file_path, data_list,
          pulse_offset, flange)
322 
323         #Calculate electron temperature linearly
324         #electron_temp = get_electron_temp_linear(double_voltage_smooth, floating_smooth)
325         Vd2_list = [double - phi_float for double, phi_float in zip(double_voltage[0],
          floating[0])]
326         Vd2_errors = [np.sqrt(double**2 + phi_float**2) for double, phi_float in
          zip(double_voltage[1], floating[1])]
327 
328         #Calculate electron temperature numerically
329         electron_temp = get_electron_temp(200, Vd2_list, Vd2_errors)
330 
331         #Calculate electron density
332         electron_density = get_electron_density(double_voltage, floating,
          double_current, electron_temp, Vd2_list, Vd2_errors)
333 
334         pd_data.append([radius,electron_temp[0], electron_temp[1], electron_temp[2],
          electron_density[0], electron_density[1]])
335     if i == 1:
336         parameter_df_1 = pd.DataFrame(pd_data, columns=['Radius', 'electron
          temp','electron temp error low','electron temp error high', 'electron density',
          'electron density errors'])
337         parameter_df_1 = parameter_df_1.set_index('Radius')
338     else:
339         parameter_df_2 = pd.DataFrame(pd_data, columns=['Radius', 'electron
          temp','electron temp error low','electron temp error high', 'electron density',
          'electron density errors'])
340         parameter_df_2 = parameter_df_2.set_index('Radius')
341     i+=1
342     # parameter_df.to_csv(r'D:/Zap_data_analysis/Thesis_data/Compiled_data/' + flange
      +'_processed_data.csv')
343 
344 
345 
346 #%%
347 '''
348 Plots given radial positions on same graph. Not useful for end wall off as there is
    only one radial data point. Must run Pandas data frame generation section
349 first
350 '''
351 '''
352 Inputs
```

```
'''
radi = [0,20,40,60,80]

################################################
legend_list = []
plt.figure()
for r in radi:
    ne = parameter_df_1.loc[r,'electron density']
    ned = parameter_df_1.loc[r,'electron density errors']
    plt.plot(time, ne)
    plt.fill_between(time, np.array(ne)-np.array(ned), np.array(ne)+np.array(ned),alpha
    = 0.2)
    legend_list.append(str(r)+' mm')
    legend_list.append(str(r)+ ' mm std')
plt.xlim([50,70])
plt.legend(legend_list,loc = 'center right', bbox_to_anchor=[1.3,0.5], title = 'Radial
Location')
plt.xlabel(r'Time [$\mu$s]')
plt.ylim([0, None])
#plt.yscale('log')
plt.ylabel(r'Electron Density [m$^{-3}$]')
#plt.title('Radial Comparison of Electron Density Time Evolution \n z=435mm')
plt.show()


#%%
'''
Calculates the Thrust and Total of ZaP-HD over time for endwall on. Need to run pandas
data frame section first
'''

'''
Inputs
'''
data = parameter_df_1
thrust_list = []
thrust_d_list = []

#End Wall On
speed = 27000 #m/s
speed_d = 13000
Ae = np.pi*0.08**2

#End Wall off
# speed = 103000
# speed_d = 6600
# Ae = np.pi*0.1**2

#Spoked End wall
# speed = 47000
# speed_d = 27700
# Ae = np.pi*0.08**2


h_mass = 1.6735575*10**-27 #kg/particle
kb = 1.38*10**-23 #J/K
keV = 8.617*10**-5 #eV/K
k = kb/keV #J/eV
mdot_list =[]
mdot_d_list = []
p0 = 0.00013 #Pa

for step in range(len(time)):
    nes = []
    nes_d = []
    Pe_list = []
    for r in range(r_start,r_end+1, rstep):
```

```
            Pe_list.append(data.loc[r,'electron density'][step]*k*data.loc[r,'electron
            temp'][step])
            nes.append(data.loc[r,'electron density'][step])
            nes_d.append(data.loc[r,'electron density errors'][step])
        Pe_avg = np.mean(Pe_list)
        Pe_std = np.std(Pe_list)
        N = np.pi*(r/1000)**2*np.mean(nes)
        mdot_list.append(N*speed*h_mass)
        N_d = np.pi*(r/1000)**2*np.mean(nes_d)
        mdot_d_list.append(N_d*speed_d*h_mass)
        thrust = h_mass*N*speed**2+(Pe_avg-p0)*Ae
        thrust_d = h_mass*N_d*speed_d**2+(Pe_std-p0)*Ae
        thrust_list.append(thrust)
        thrust_d_list.append(thrust_d)


mdot_avg = np.mean(mdot_list)
mdot_std = np.mean(mdot_d_list)
mass = mdot_avg*100*10**-6
mass_d = mdot_std*100*10**-6
timpul = simpson(thrust_list,dx = 4*10**-9)
timpul_d = simpson(thrust_d_list,dx = 4*10**-9)
isp = (timpul)/(mass*9.81)
isp_d = (timpul_d)/(mass_d*9.81)

plt.figure()
plt.plot(time, thrust_list, color = 'black')
#plt.title('ZaP-HD Estimated Thrust \n End Wall On')
plt.text(80,2.5, 'Total Impulse = ' + str('%.2E' % Decimal(timpul)) +'\n+/- ' +
str('%.2E' % Decimal(timpul_d)) + ' N-sec')
plt.text(80,2, 'Specific Impulse = ' + str(round(isp,2)) + '\n+/- ' +
str(round(isp_d,2)) + ' sec')
plt.fill_between(time, np.array(thrust_list) - np.array(thrust_d_list),
np.array(thrust_list) + np.array(thrust_d_list), alpha = 0.2, color = 'grey')
plt.xlabel('Time (us)')
plt.ylabel('Thrust (N)')
plt.ylim([0,None])
plt.grid()
plt.show()


#%%
'''
Makes an approximate I-V trace for a given radial position and time
'''
'''
Inputs
'''
position = [0, 'Second Flange']
data_list = make_shot_list(position, 'On')
t = 69
pulse_offset = 2000
file_path = 'D:/Zap_data_analysis/Thesis_data/Lab_data/End Wall On/'

#####################################################
mi = 1.6726*10**-27
r_probe = 0.025*2.54*0.01 # Probe radius (m)
l_probe = 0.066*2.54*0.01 # Probe length (m)
S = (np.pi*r_probe**2 + l_probe*np.pi*2*r_probe)
e = 1.602*10**-19
kb = 1.38*10**-23 #J/K
keV = 8.617*10**-5 #eV/K
k = kb/keV #J/eV


# Get the data
floating, double_voltage, double_current, time = avg(file_path, data_list,
```

```
    pulse_offset, position[1])
480
481 #Calculate electron temperature linearly
482 #electron_temp = get_electron_temp_linear(double_voltage_smooth, floating_smooth)
483 Vd2_list = [double - phi_float for double, phi_float in zip(double_voltage[0],
    floating[0])]
484 Vd2_errors = [np.sqrt(double**2 + phi_float**2) for double, phi_float in
    zip(double_voltage[1], floating[1])]
485
486 #Calculate electron temperature numerically
487 electron_temp = get_electron_temp(200, Vd2_list, Vd2_errors)
488
489 electron_density = get_electron_density(double_voltage, floating, double_current,
    electron_temp, Vd2_list, Vd2_errors)
490
491 t_diff = np.absolute(time-t)
492 t_index = t_diff.argmin()
493 eV = electron_temp[0][t_index]
494 Isat = 0.61*electron_density[0][t_index]*e*S*np.sqrt(k*eV/mi)#double_current[0][t_index]
495 m = np.exp(1/eV)
496 vf = floating[0][t_index]
497 vs2 = np.linspace(vf,10,100)
498 vs1= np.linspace(-10,vf,100)
499 b = -m*vf
500 y = m*vs2+b
501 ye = np.exp(5*vs1)-Isat
502 plt.figure()
503 plt.plot(vs1,ye,color = 'green')
504 plt.plot(vs2,y, color = 'green')
505 plt.xlim([-5,5])
506 plt.ylim([-1,5])
507 plt.title('Reconstructed I-V Characteristic \n R=' + str(position[0]) + ', ' +
    position[1] + ', Time=' + str(t) + ' us')
508 plt.xlabel('Bias Voltage (V)')
509 plt.ylabel('Probe Current (A)')
510 plt.text(-4,3.5, 'Te=' + str(round(eV,2)) + ' eV')
511 plt.show()
512
513
514
515
516
517
518
519
520
521
522
523
524
525
526
527
528
529
530
531
532
533
534
535
536
537
```

B.3 IDS Code

```python
# -*- coding: utf-8 -*-
"""
Created on Wed Apr 12 13:36:44 2023

Analyzes the data from LightField and plots the speed distribution

@author: Jared
"""

import spe_loader as spe
import os
import matplotlib.pyplot as plt
import numpy as np
from statistics import mean
from scipy.signal import find_peaks, peak_widths
from scipy.optimize import curve_fit
import pandas as pd

plt.rcParams['axes.grid'] = False

def bin_data_ave(data, edge_of_bins):
    '''
    Averages each chord by finding the middle, then averaging over
    the 10 pixels above and below that
    '''
    # Bins data
    N_rows = int(len(edge_of_bins) / 2)
    data = np.asarray(data)
    binned_data=np.zeros([len(edge_of_bins) // 2, data.shape[1]])

    for row_iterator in range(N_rows):
        lower_edge_of_bin = edge_of_bins[2*row_iterator]
        upper_edge_of_bin = edge_of_bins[2*row_iterator + 1]
        middle_of_bin = int(np.rint((upper_edge_of_bin - lower_edge_of_bin)/2))
        lower_edge_of_ave = lower_edge_of_bin + middle_of_bin - 10
        upper_edge_of_ave = upper_edge_of_bin - middle_of_bin + 10

        binned_data[row_iterator,:] = np.mean(data[lower_edge_of_ave:upper_edge_of_ave,
        :], axis=0)
        bkg_value = np.amin(binned_data[row_iterator,:])
        binned_data[row_iterator,:] = binned_data[row_iterator,:] - bkg_value

    return binned_data


def linear(x, m,b):
    return m*x+b


def calibration(calibration_file, chord_num, bin_edges):
    """
    Creates a list that maps pixel space to wavelength space. Need a spectra file from
    a Cd pen lamp
    looking at the 226.5 nm line and the 228.8 nm line
    """
    known_wavelengths = [226.5019,228.80227]
    calfile = spe.SpeFile(calibration_file)
    frame = calfile.data
    cal_data_int = bin_data_ave(frame[0][0], bin_edges)
    chord = cal_data_int[chord_num,:]
    height = mean(chord)
    peaks, prop = find_peaks(chord, height = height, prominence = 0.75*height)
    width_parms = peak_widths(chord, peaks, rel_height = 0.5)
    centroids = [int((width_parms[3][0] + width_parms[2][0])//2),
    int((width_parms[3][1] + width_parms[2][1])//2)]
    parms, cov = curve_fit(linear, centroids, known_wavelengths)
    data_wave = linear(range(1024), parms[0], parms[1])
```

```
    # plt.figure()
    # plt.plot(data_wave, chord)
    # plt.title('Cd I and Cd II Calibration Lines')
    # plt.xlabel('Wavelength (nm)')
    # plt.ylabel('Intensity (Arb)')
    # #plt.plot(centroids, chord[centroids], '*')
    # plt.axvline(226.5, ls = '--', lw = 1)
    # plt.axvline(228.8, ls = '--', lw = 1)
    #plt.xlim([228.7, 229])
    #plt.ylim([0,3000])
    #plt.plot([width_parms[2][1],width_parms[3][1]],[width_parms[1][1],
    width_parms[1][1]])
    return data_wave, cov


def speed(data, calfile, bin_edges):
    '''
    Calculates ion speed from the doppler shift. Using per chord calibration
    '''
    speed_list = []
    c = 3*10**8
    lambda_not = 229.687
    for chord_num, chord in enumerate(data):
        data_wave, cov = calibration(calfile, chord_num, bin_edges)
        pixel_max = np.where(chord == max(chord))[0][0]
        width_parms = peak_widths(chord, [pixel_max], rel_height = 0.5)
        pixel_prime = (width_parms[3] + width_parms[2])/2
        lambda_prime = data_wave[round(pixel_prime[0])]
        # plt.figure()
        # plt.plot(data_wave, chord)
        # plt.plot(lambda_prime, width_parms[1], '*')
        # print(lambda_prime)
        if 229.4 < lambda_prime < 229.9:
            # plt.plot(lambda_prime, width_parms[1], '*')
            speed =
            (c*((abs(lambda_not-lambda_prime))/lambda_not)*(1/np.cos(np.deg2rad(35))))/10
            00
            speed_list.append(speed)
        else:
            speed_list.append(np.nan)
    return speed_list


# On is from 230306. Off is from 230405 Spoked is 230522
folder_path = 'D:/Thesis_things/Data/IDS/2023_5_22'
calfile = 'D:/Thesis_things/Data/IDS/Calibration_for_CIII.spe'
bin_edges1 =
[0,30,80,130,180,230,270,330,380,430,480,530,580,630,680,730,780,830,880,920]
bin_edges2 =
[30,80,130,180,230,270,330,380,430,480,530,580,630,680,730,780,830,880,920,980]
impact_para = [-10, -8, -6, -4,-2, 2,4,6,8,10]
speed_front_df = pd.DataFrame(columns = impact_para)
speed_aft_df = pd.DataFrame(columns = impact_para)

for filename in os.listdir(folder_path):
    f = os.path.join(folder_path, filename)
    if os.path.isfile(f):
        spe_file = spe.SpeFile(f)
        for frame_index, frame in enumerate(spe_file.data):
            data_full_frame = frame[0]

            # plt.figure()
            # plt.pcolormesh(np.arange(1,1025,1.0),range(int(spe_file.ydim[0])),
            data_full_frame, shading='auto')
            # [plt.axhline(bin_edge, color='w', linewidth='0.5') for bin_edge in
            bin_edges1]
            # plt.ylabel('Pixel')
```

```
            # plt.xlabel('Pixel')
            # plt.title('Shot 230405013 C III Emission')

            data_int1 = bin_data_ave(data_full_frame, bin_edges1)
            data_int2 = bin_data_ave(data_full_frame, bin_edges2)

            speed1 = speed(data_int1, calfile, bin_edges1)
            speed2 = speed(data_int2, calfile, bin_edges2)

            speed_front_df.loc[len(speed_front_df.index)] = speed1
            speed_aft_df.loc[len(speed_aft_df.index)] = speed2



speed_front_avgs = speed_front_df.mean()
speed_front_std = speed_front_df.std()
speed_aft_avgs = speed_aft_df.mean()
speed_aft_std = speed_aft_df.std()
speed = np.mean([speed_front_avgs,speed_aft_avgs],axis=0)
std = np.mean([speed_front_std,speed_aft_std],axis=0)
plt.figure()
plt.errorbar(impact_para, speed, std, color = 'blue', marker = '.')
#plt.errorbar(impact_para,speed_aft_avgs, speed_aft_std, color = 'blue',marker = '.')
plt.xticks([-10, -8, -6, -4,-2, 0,2,4,6,8,10])
plt.xlabel('Impact Parameter (mm)')
plt.ylabel('Speed (km/s)')
#plt.ylim([0,100])
plt.grid()

plt.show()
```